This is a repository copy of *An integrated modelling approach for the seismic collapse assessment of masonry towers*.

White Rose Research Online URL for this paper:
https://eprints.whiterose.ac.uk/194492/

Version: Published Version

An Integrated Modelling Approach for the Seismic Collapse Assessment of Masonry Towers

Anjali Mehrotra, Andrew Liew, Philippe Block & Matthew J. DeJong

Published online: 01 Nov 2022.

Submit your article to this journal ⬚

Article views: 280

View related articles ⬚

View Crossmark data ⬚

Taylor & Francis
Taylor & Francis Group

An Integrated Modelling Approach for the Seismic Collapse Assessment of Masonry Towers

Anjali Mehrotra [a], Andrew Liew[b], Philippe Block[c], and Matthew J. DeJong [d]

aFaculty of Civil Engineering and Geosciences, Delft University of Technology, Delft, The Netherlands; bDepartment of Civil and Structural Engineering, University of Sheffield, Sheffield, UK; cInstitute for Technology in Architecture, Block Research Group – Institute for Technology in Architecture, ETH Zurich, Switzerland; dDepartment of Civil and Environmental Engineering, University of California - Berkeley, Berkeley, California, USA

ABSTRACT

Failure of tall slender masonry structures during earthquakes often involves partial collapse of the structure well-above ground level. Consequently, the elastic response of the structure needs to be considered, which often requires modal analysis using finite element models — the generation of which can be labour-intensive and time-consuming. This paper presents a new integrated modelling approach which combines finite element analysis with rocking dynamics to model the seismic response of complex structural geometries in a computationally-efficient manner. The modelling strategy is implemented within the open-source computational framework COMPAS and is incorporated within the broader framework of a tool being developed for the seismic collapse assessment of masonry structures. The framework of this tool is first outlined, and the utility of the new modelling approach then demonstrated through application to the seismic assessment of a three historic masonry towers in North-Eastern Italy. The importance of accounting for elastic amplification effects, as well as the influence of varying boundary conditions on the dynamic response, is also illustrated.

1. Introduction

Masonry structures are susceptible to collapse under the influence of seismic action. When such structures fail, they often do so via specific, well-documented collapse mechanisms (D'Ayala and Speranza 2002; PCM-DPC MiBAC 2006). In the case of tall slender structures such as masonry towers, these mechanisms often include overturning of elements such as pinnacles and gables, partial collapse of spires, rocking of the belfry, and extensive vertical and diagonal cracking in the shaft of the tower leading to corner failure (PCM-DPC MiBAC 2006).

Analysis of the collapse of these structures can be conducted using either simplified procedures such as limit analysis (Heyman 1992; Sarhosis et al. 2018; Torelli et al. 2020) as implemented for example in the Italian building code (DMI 2008), or using more complex numerical modelling strategies such as finite element analyses (Castellazzi et al. 2018; Milani and Clementi 2021; Peña et al. 2010; Shakya et al. 2018; Shehu 2022; Torelli et al. 2020; Valente and Milani 2016b, 2016a) or distinct element methods (Azevedo, Sincraian, and Lemos 2000; Clementi et al. 2020; Ferrante, Clementi, and Milani 2020; Ferrante et al. 2021; Pulatsu, Gencer, and Erdogmus 2020; Sarhosis et al. 2018). While the analytical methods can be over-conservative, often underestimating dynamic capacity and leading to expensive — and at times unnecessary — retrofitting solutions, the numerical models can be computationally-expensive and time-consuming, especially when trying to model collapse.

As an alternative analysis approach, rocking dynamics, whereby equations of motion describing different collapse mechanisms are directly derived and solved, can be used instead (Housner 1963). This approach has been applied to the analysis and assessment of a variety of structures including masonry walls (Doherty et al. 2002; Sorrentino, Masiani, and Griffith 2008; Sorrentino et al. 2008; Al Shawa et al. 2012; Mauro, de Felice, and DeJong 2015; Lagomarsino 2015; Giresini and Sassu 2017; Mehrotra and DeJong 2018), arches (Clemente 1998; DeJong et al. 2008; DeJong and Ochsendorf 2006; De Lorenzis, DeJong, and Ochsendorf 2007; Oppenheim 1992), portal frames (Allen et al. 1986; DeJong and Dimitrakopoulos 2014; Makris and Vassiliou 2013), spires (DeJong 2012) and monuments (Mehrotra and DeJong 2017), and has also been incorporated into different building codes

CONTACT Anjali Mehrotra · A.A.Mehrotra@tudelft.nl · Faculty of Civil Engineering and Geosciences, Delft University of Technology, Building 23, Stevinweg 1, 2628 CN, Delft, The Netherlands

(American Society of Civil Engineers (ASCE) 2007; DMI 2008; DeJong 2014). Such an approach has the advantage of being less computationally-demanding than most numerical models, while providing more accurate predictions than most simplified analytical methods.

Additionally, assessment of real structures often requires consideration of numerous different collapse mechanisms, many of which involve partial collapse of the structure well above ground level. Thus, amplification and filtering of the ground motion by the building, which depends in turn on the natural frequency of the structure, also needs to be taken into account (Priestley 1985). While the natural frequency and modes of simple, regular structures can be determined analytically, for many historic structures (e.g. bell towers, churches) consideration of the elastic response requires modal analysis using finite element models, the generation of which can be labour-intensive and time-consuming.

In this paper, a new integrated modelling approach — which requires only a 3D CAD model of the structure as input — is presented, which combines finite element analysis with rocking dynamics to model the seismic response of complex geometries in a computationally-efficient manner. The modelling strategy is implemented within COMPAS, an open-source computational framework that provides geometry processing independent of CAD software (Van Mele and many others, 2017–2021), and is incorporated within the broader framework of a tool being developed for the seismic collapse assessment of masonry structures (Mehrotra and DeJong 2018). To keep the solution strategy open-source, modal analyses are conducted using the *compas_fea* package (Liew and Mendez Echenagucia 2017), which directly constructs the FE model from the input geometry, and analyses it using the open-source finite element solver *OpenSees* (McKenna et al. 2000). The results of the modal analysis are subsequently used to define an equivalent single-degree-of-freedom (SDF) oscillator, which is subjected to different ground motion records. The response of the oscillator is then scaled appropriately using the mode shape, and the scaled response is then used as the input signal at the base of the rocking mechanism. The procedure can be repeated for a wide range of potential collapse mechanisms within a structure to determine the most vulnerable mechanisms for a given suite of ground motions. The utility of this new modelling approach is finally demonstrated by applying it to the seismic assessment of a three historic masonry towers in North-Eastern Italy.

2. Methodology

A flowchart outlining the functioning of this proposed tool can be found in Figure 1. As Figure 1 illustrates, the tool first takes as input the mechanism geometry in Rhino. This geometry is then converted into a COMPAS mesh, and the parameters defining the rocking equation of motion for this mechanism are calculated and provided as output. In the case of mechanisms that take place at ground level, the solution procedure is fairly straightforward. For full time-history analyses, the rocking equation of motion is directly solved for the selected input ground motion a_g, while for pulse response analyses the overturning plots are generated using the equivalent rocking parameters as calculated above. In the case of mechanisms that take place above ground level (i.e. $h_m > h_g$) on the other hand, modal analyses are first conducted using the *compas_fea* package, which provides as output the corresponding frequencies and mode shapes for the structure, which in turn are used to transform the structure into an equivalent SDF oscillator. In case a full time-history analysis is desired, this SDF oscillator is solved for the selected input ground motion a_g, to get the filtered and scaled acceleration $a_{g,rock}$ expected at the base of the mechanism h_m. This acceleration serves as input for the rocking equation of motion, which is then solved to obtain the maximum response of the structure. Alternatively, if a pulse response analysis is required, the overturning plots are generated as above, and the SDF oscillator is then solved for sine pulses of varying frequency to obtain the scaled pulse response spectrum (PRS). This PRS is then used to scale the overturning plots to finally yield the seismic capacity of the mechanism.

2.1. Geometry and mechanism definition in the CAD interface

As stated in the introduction, the proposed modelling strategy only requires a 3D CAD model of the structure as input. However, as this strategy is implemented within COMPAS, which is a Python-based framework, it is crucial that the CAD program used is capable of editing and executing Python-based scripts. To that end, the CAD program Rhino (Robert McNeel & Associates 2014) was selected as the preliminary interface for this tool as it comes with its own Python interpreter.

Once the geometry of the whole structure has been defined in Rhino, the portion of the structure involved in the collapse mechanism needs to be specified. Note that the accuracy of the proposed methodology depends in large part upon the correct choice of this mechanism, which often comes down to user experience and engineering judgment. The mechanism geometry is first defined as a 3D closed polysurface (solid), which is then meshed in Rhino. The *compas_rhino.helpers* package is subsequently used to convert the Rhino mesh into
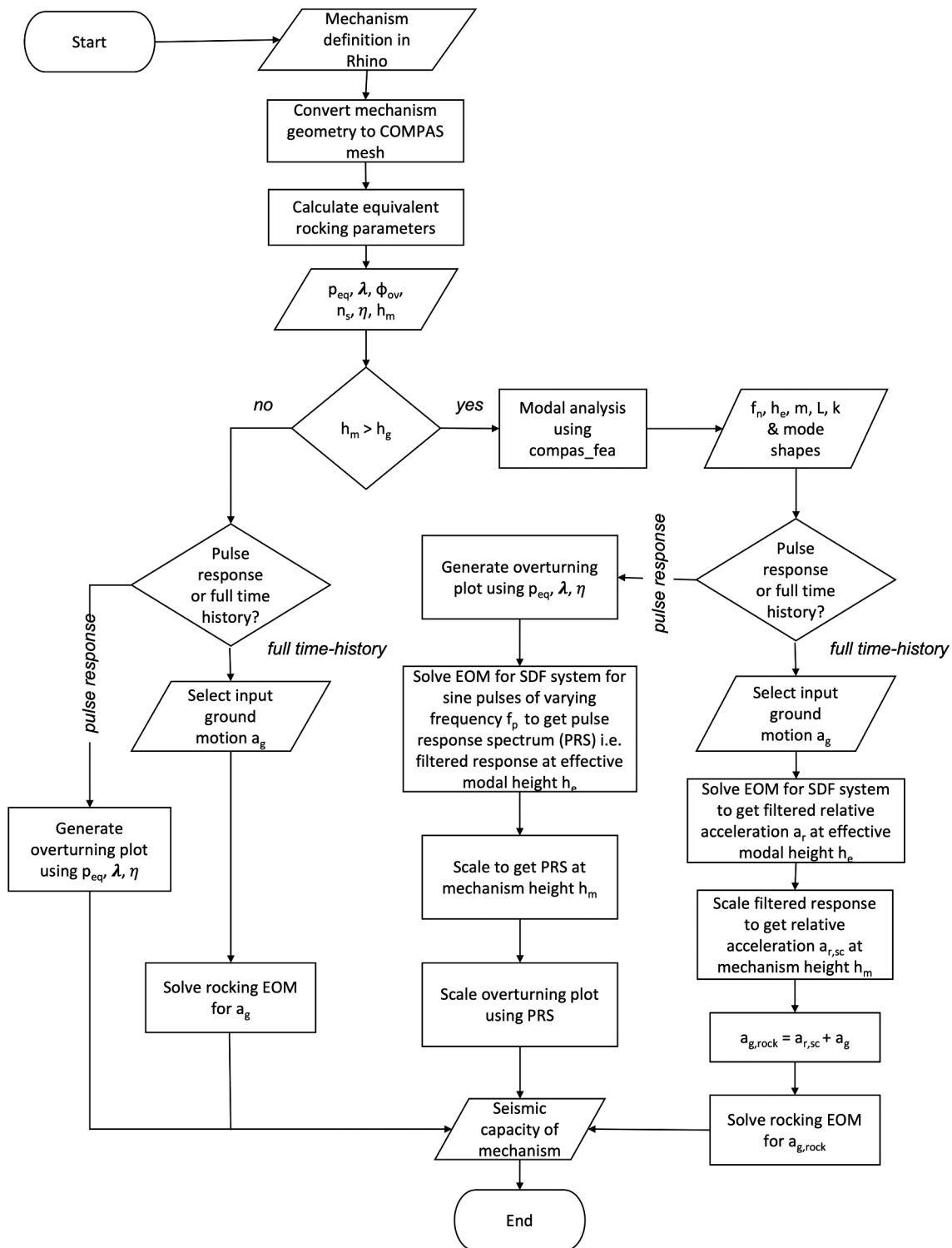
Figure 1. Flowchart illustrating the functioning of the proposed computational tool/modelling approach.

its COMPAS counterpart, resulting in a 2D mesh data structure defined by a set of vertices and faces (see Figure 2, right). The axis of rocking rotation, as defined by the user, is also saved as an attribute of this mesh so that it can be easily accessed in the next stage of analysis. If the mechanism takes place above ground level,

a second mesh comprising the entire structure is also created and converted into its COMPAS counterpart (Figure 2, left). As this second mesh serves as the basis of the finite element model used for the modal analysis, a suitably fine mesh size should be used to obtain reasonable results.

Figure 2. Geometry and mechanism definition in Rhino, and conversion to corresponding COMPAS meshes.

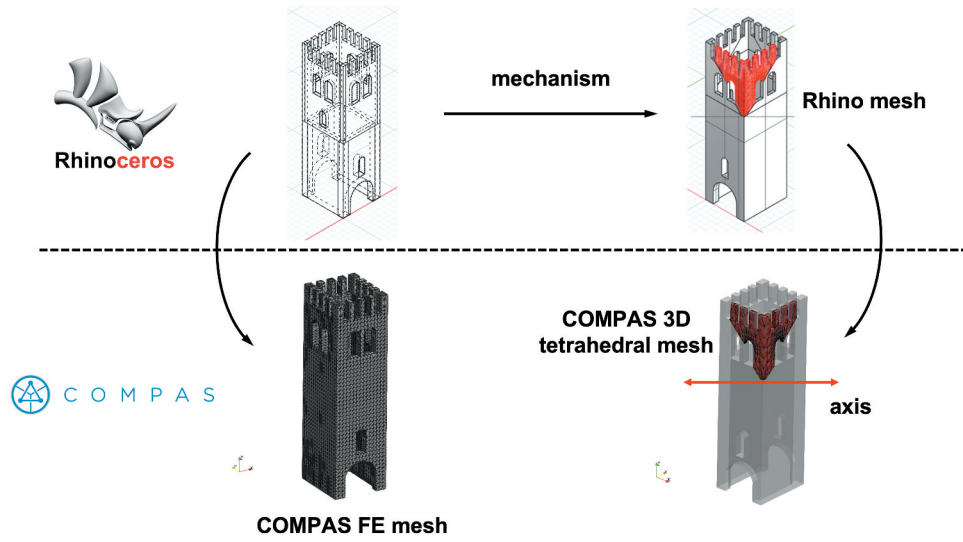As mentioned earlier, the mesh data structures exported from Rhino comprise only 2D face meshes, i.e. only the external faces of the solids are meshed. These meshes first need to be converted into 3D tetrahedral meshes (i.e. internally meshed) before any operations can be performed on it within the COMPAS framework. This is done using the package MeshPy (Klöckner 2008), which in turn provides a Python interface to program TetGen (Si 2015).

2.2. Calculation of equivalent rocking parameters

Once the mechanism geometry has been converted to the 3D mesh data structure, geometric operations can be directly performed on it within the COMPAS environment. These include extraction of the various geometric properties (such as moment of inertia, volume and centre of mass) that are used to define the rocking equation of motion, which assumes the following general linearised form (Mauro, de Felice, and DeJong 2015):

$$\tilde{I}\ddot{\Phi} - \tilde{K}(\Phi - \Phi_{cr}) = -\tilde{B}\ddot{u}_g + \tilde{M} \qquad (1)$$

where $\tilde{I}$, is the moment of inertia of collapsed portion of the structure about the axis of rotation, $\tilde{M}$ is the moment caused by the external static forces, ϕ_{cr} is the critical rotation, $\tilde{K}$ is the rotational stiffness of the system, and $\tilde{B}\ddot{u}_g$ is the moment provided by the ground motion applied to the structure. Note that the linearisation of this equation is about the point of unstable equilibrium (i.e. $\phi = \phi_{cr}$, following the approach first proposed by Housner (1963) for tall slender structures) in order to obtain local dynamic equivalence with the single rocking block. This single equation of motion can then be used to describe a variety

of different mechanisms, ranging from the overturning of a single rocking block to the dynamic behaviour of more complex two and three block mechanisms. These linearised equations tend to decrease in accuracy as block slenderness decreases. However, for single block mechanisms, Allen and Duan (1995) found the error associated with linearisation to be less sensitive to slenderness and more sensitive to the scale of the blocks. These findings were corroborated by DeJong and Dimitrakopoulos (2014) for two and three block mechanisms, where the errors evaluated for blocks of varying slenderness were found to be acceptable — particularly when considering the relatively large uncertainties generally associated with the prediction of earthquake ground motion.

By using the following transformation of variables:

$$\theta = \Phi \frac{\tilde{K}}{g\tilde{B}} \qquad (2)$$

Equation (1) can thus be rewritten as:

$$\ddot{\theta} = p_{eq}^2 \left(\theta - \lambda - \frac{\ddot{u}_g}{g} \right) \qquad (3)$$

where p_{eq} is the rocking frequency parameter and λ is an approximation of the static load multiplier that activates the mechanism. Both these terms depend on the kinematic constants $\tilde{I}$, $\tilde{K}$, $\tilde{B}$, $\tilde{M}$ and ϕ_{cr}, which in turn depend on both the geometry of the structure as well as the type of collapse mechanism; more detailed expressions for which can be found in Mehrotra and DeJong (2018).

Additionally, the overturning rotation ϕ_{ov}, that is, the rotation upon the exceedance of which the structure will overturn and collapse, can also be calculated using the aforementioned kinematic constants as shown below:

$$\phi_{ov} = \phi_{cr} - \frac{\tilde{M}}{\tilde{K}} \qquad (4)$$

If the structure does not overturn but the rotation angle returns to zero, impact occurs. During impact, energy dissipation is accounted for through the coefficient of restitution η, which depends not only on the geometry of the blocks but also on the type of rocking, i.e. one-sided ($n_s = 1$) or two-sided ($n_s = 2$). For more detailed expressions for the coefficient of restitution, please refer to Mehrotra and DeJong (2018). Finally, the height h_m at which the mechanism occurs is determined by taking the average of the heights of the two points defining the axis of rotation, previously saved as an attribute of the mesh.

2.3. Modal analysis using compas_fea

In the case of mechanisms that take place above ground level (i.e. $h_m > h_g$) modal analyses need to be conducted to define an equivalent single-degree-of-freedom elastic oscillator, which in turn is used to account for the amplification and filtering of the ground motion by the structure.

Using the tetrahedral mesh of the entire structure as generated in Section 2.1, the compas_fea package is utilised for the construction of the corresponding finite element model. To do this, a Structure object is first created, with nodes corresponding to each of the points of the tetrahedral mesh and elements corresponding to each of the tetrahedral elements. Material properties are set through the assignment of a material type (for the purpose of the analyses in this paper, elastic isotropic) which in turn is characterised by a user-defined Young's modulus, Poisson's ratio and density. Loads and displacements are then applied by means of Step objects, which provide instructions to the finite element solver about the type and order of the different analysis stages. Boundary conditions are first specified through the creation of an initial Step object, which assigns pinned displacements to predefined node sets. A second Step object, in this case ModalStep, is then added to instruct the finite element solver to conduct a modal analysis, specifying the number of modes to be analysed.

After the Structure object has been constructed, it is written to a .tcl input file which is subsequently sent to OpenSees for analysis. The analysis is conducted in the background and once completed, the results — such as the fundamental frequency f_n and nodal displacements u — are returned. Post-processing of this data results in the structure being transformed into an equivalent single-degree-of-freedom elastic oscillator, defined by the following equation of motion:

$$\tilde{m}\,\ddot{z} + 2\,\tilde{m}\,\xi\omega_n\dot{z} + \tilde{k}\,z = -\tilde{L}\,\ddot{u}_g \qquad (5)$$

where:

$$\tilde{m} = \sum_{i=1}^{N} m_i u_i^2; \tilde{L} = \sum_{i=1}^{N} m_i u_i;$$
$$\omega_n = 2\pi f_n \quad and \quad \tilde{k} = \tilde{m}\omega_n^2 \qquad (6-9)$$

where N is the total number of nodes in the model, m_i is the mass lumped into each of them, and u_i their corresponding displacements. System damping is specified through the term ξ, and is set to 5% for the analyses conducted in this paper. Solving Equation (5) gives the response of the oscillator at the effective modal height h_e, which is determined using the following expression:

$$h_e = \frac{\sum_{i=1}^{N} m_i u_i h_i}{\sum_{i=1}^{N} m_i u_i} \qquad (10)$$

where h_i is the height of each node. However, for mechanisms that occur at a height above or below h_e (i.e. $h_m \neq h_e$), the response needs to be scaled using the mode shapes, which are extracted using the nodal displacements u. This is illustrated by Figure 3 for a sample tower with varying boundary conditions. Two cases are considered: an isolated case where only base nodes are pinned, and a fixed case where nodes on either side of the structure are also pinned up to a certain height, to simulate the connectivity of the tower to adjacent buildings.

Note that two simplifications are made here. The first is that only the fundamental modes in each direction are considered. This simplification was made for four reasons: 1) the fundamental mode has the lowest frequency, and low frequency motions are known to cause large rocking response, 2) for all of the towers considered in this paper, modal analysis indicated that the fundamental modes in each direction account for the majority of the participating mass, 3) Valente and Milani (2016a) found that higher modes only contributed significantly to the response of slender towers when substantial irregularities were present, which is not the case for the structures considered here, and 4) to keep the modelling approach as simple as possible. However, higher mode contributions could still be important in the rocking collapse of some tall slender towers. The proposed modelling strategy could readily incorporate the effect of higher modes using the same procedure, either by treating those higher modes independently, or by using modal superposition in the process of translating the motion at the base of the structure to the motion at the base of the mechanism.
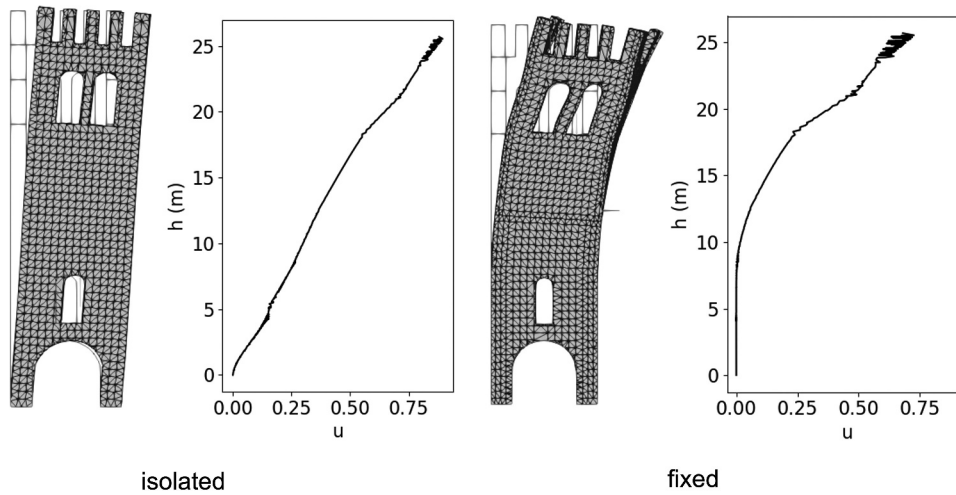
Figure 3. First mode shapes extracted by the tool for a sample tower, for both the isolated case as well as the case where the tower is connected to the adjacent buildings ("fixed" case).

The second assumption is that the structural response is linear, even though, after activation of the mechanisms, the modes would change. This assumption is made to maintain the objective of a simple and computationally efficient modelling strategy. In addition, in general, the change in modes would be characterised by an increase in frequency due to the smaller mass and reduced height of the remaining portion of the structure. Consequently, the filtered ground motion would be characterised by a higher frequency content which is, in general, less destructive for rocking structures. Given that rocking systems display a high vulnerability to ground motions with lower frequency contents (Mehrotra and DeJong 2017), the assumption that the modes do not change (i.e. the lowest frequency modes are retained) should yield conservative results.

2.4. Full time-history analysis

When full time-history analyses are desired, Equation (5) is first solved for the unscaled input ground acceleration a_g (i.e. $\ddot{u}_g = a_g$, Figure 4(a). The solution to the equation of motion yields the filtered acceleration response of the structure a_r (relative to the ground) at the effective modal height h_e (Figure 4(b). For mechanisms that occur at a height other than h_e ($h_m \neq h_e$), a_r then needs to be scaled following the approach proposed by Priestley (1985), by extrapolating using the mode shapes obtained from the modal analyses (Figure 3) to get the filtered and scaled response $a_{r,sc}$ at the mechanism height h_m (Figure 4(c)):

$$a_{r,sc} = \frac{u(h_m)}{u(h_e)} a_r \qquad (11)$$

However, $a_{r,sc}$ is only the scaled and filtered response of the structure relative to the ground. Thus to get the total acceleration experienced by the structure at the base of the rocking mechanism, this acceleration $a_{r,sc}$ is added to the original input ground acceleration a_g and the final combined acceleration is illustrated by Figure 4(d). This acceleration $a_{g,rock}$ serves as the final input signal for the rocking equation of motion (i.e. in Equation (3) $\ddot{u}_g = a_{g,rock}$), which is then solved to predict the response of the rocking mechanism in terms of rotation ϕ over time.

2.5. Pulse response

As an alternative to full time-history analyses, pulse response analyses can also be conducted to predict the response of the structure to single sinusoidal pulses of varying frequency f_p and amplitude a_p. The results of these analyses are presented using overturning plots as illustrated by Figure 5 (for the dimensionless case), which indicate, for a pulse of a given frequency f_p and amplitude a_p, whether the mechanism (characterised by a certain p_{eq} and λ) will overturn without impact, with a single impact, or not overturn at all. These plots can be particularly useful when analysing how a structure responds to near-source ground motions, which have been found to be well-represented by trigonometric pulses (Iwan and Chen 1994; Makris and Roussos 1998, 2000), as well as for comparing the relative dynamic resilience of different collapse mechanisms within a structure (Dimitrakopoulos and DeJong 2012). Generation of the plots by the tool is relatively quick, due in part to a pre-generated library of dimensionless plots, one of which can be selected for two-sided
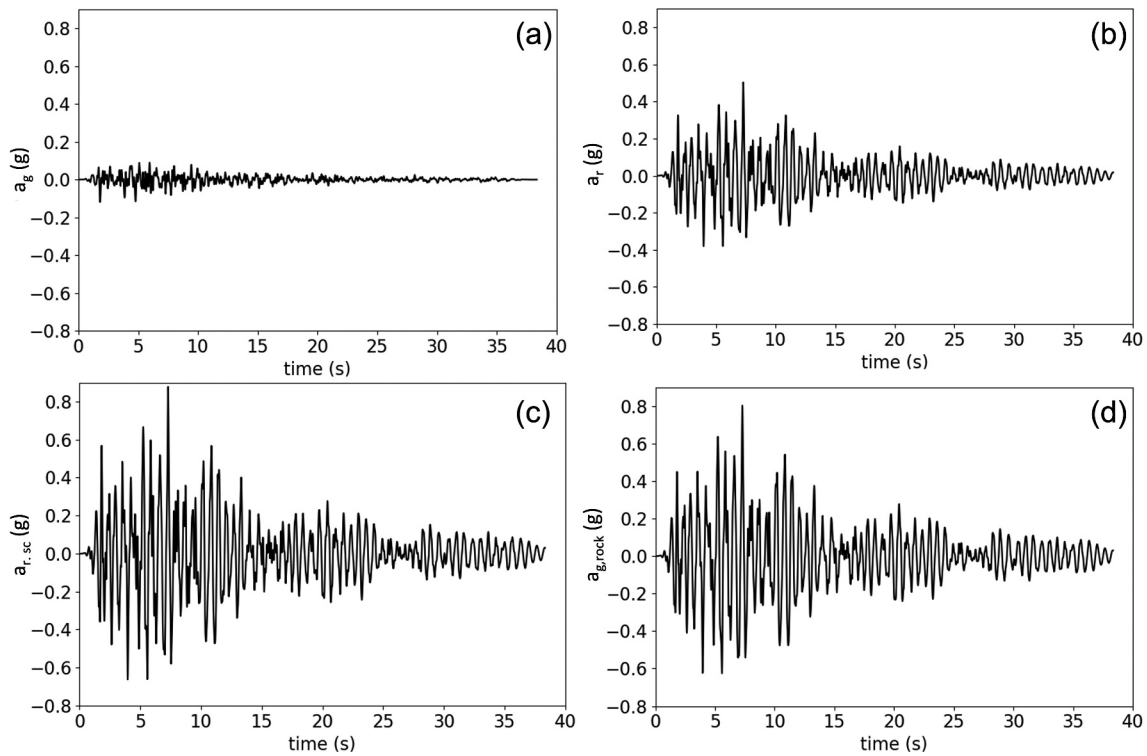
Figure 4. Procedure for filtering and scaling of the input ground motion: (a) unscaled input ground acceleration a_g, (b) filtered relative acceleration a_r at the effective modal height h_e, (c) scaled and filtered relative acceleration $a_{r,sc}$ at the mechanism height h_m and (d) final input signal at base of rocking mechanism $a_{g,rock}$.
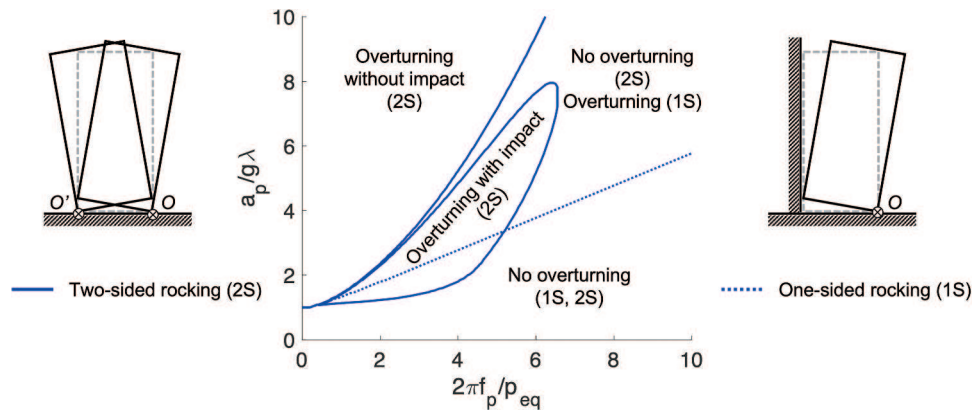

Figure 5. Dimensionless overturning plots for both one-sided and two-sided rocking (shown here for $\eta = 0.90$ for the two-sided case).

rocking based on the coefficient of restitution η (shown in Figure 5 for $\eta = 0.90$) . Note that for one-sided rocking the dimensionless plot is independent of η, as it is assumed that positive pulse overturning without impact governs, which has been found to be the case for most practical one-sided mechanisms (Mauro, de Felice, and DeJong 2015; Mehrotra and DeJong 2018). The dimensionless plots then only need to be scaled by the rocking parameters p_{eq} and λ to obtain dimensional overturning envelopes. For a more detailed explanation of this procedure, please refer to Mehrotra and DeJong (2018).

In the case of mechanisms which occur above the ground ($h_m > h_g$) these plots also need to be scaled to account for the amplification and filtering of the pulses by the structure. To do this, pulse response spectra (PRS) are first generated by solving Equation (5), now replacing $\ddot{u}_g$ with a sinusoidal pulse with amplitude a_{pg} and frequency f_p. The maximum relative acceleration $a_{r,max}$ predicted by Equation (5), normalised by the input pulse acceleration a_{pg} is then plotted against the pulse frequency f_p, normalised by the fundamental frequency of the structure f_n (Figure 6(a)). As in the case of
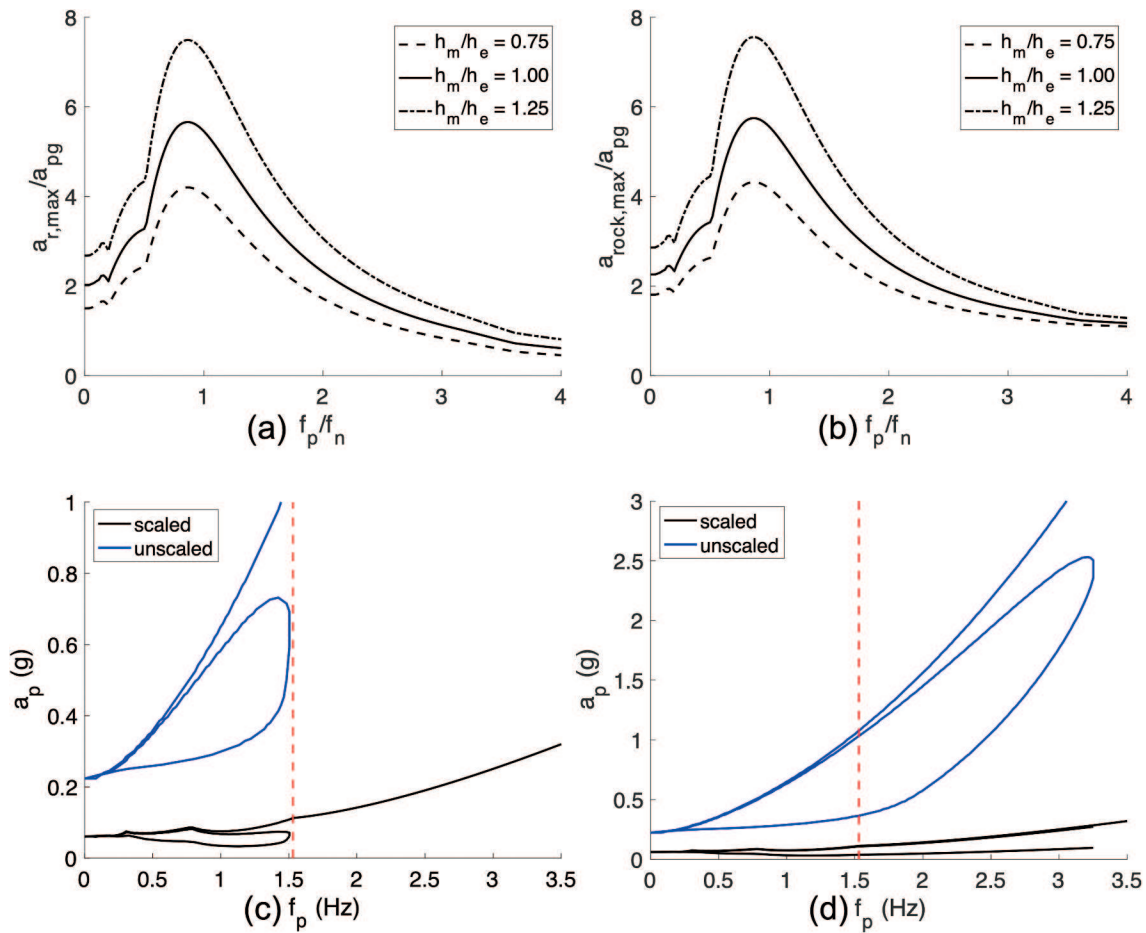
Figure 6. Procedure for scaling the overturning envelopes: (a): generation of the pulse response spectra; (b): scaled pulse response spectra; (c): scaling of the overturning plots for the case where overturning with impact occurs for only frequencies less than the natural frequency f_n of the structure (left) and frequencies both less than and greater than f_n (right) (shown here for a sample mechanism undergoing two-sided rocking, with $p_{eq} = 2.55$, $\lambda = 0.22$, $f_n = 1.53$ Hz, $\tilde{L}/\tilde{m} \approx 2$, and $\eta = 0.75$ (c) and 0.93 (d)).

the full time-history analyses, this response is at the effective modal height h_e. Thus to generate the PRS for mechanisms at other heights, the response $a_{r,max}$ also needs to be scaled using the mode shapes as in the previous subsection. Finally as this is only the response relative to the ground, it is combined with the input ground motion a_{pg} using the square-root-sum-of-squares approach as outlined in Priestley (1985), in order to get the total maximum acceleration $a_{rock,max}$ experienced at the base of the mechanism (Figure 6(b)).

This scaled pulse response spectra (Figure 6(b)) is then used to scale the original overturning plots (indicated by the blue lines in Figure 6(c,d)). For pulses with frequencies $f_p < f_n$, the plots are scaled by simply dividing the original value of a_p by the ratio $a_{rock,max}/a_{pg}$ for a given value of f_p, while for pulses with frequencies greater than f_n, the plots are scaled by dividing the original value of a_p at $f_p = f_n$ by the ratio $a_{rock,max}/a_{pg}$, as the structure will respond at its natural frequency for higher frequency pulses. Note that

for mechanisms where pulses with frequencies greater than or equal to f_n result in overturning with impact, the scaled plots (shown in black in Figure 6(c,d)), for $f_n = 1.53$ Hz) now "open" up as illustrated by Figure 6(d), and in this case only the lower bound of these plots needs to be considered.

3. Application: analysis of three historic masonry towers

To demonstrate this new integrated modelling approach, three historic masonry towers from northeastern Italy were chosen as case studies. Incremental dynamic analyses were conducted for a predefined set of collapse mechanisms for each of the towers, while overturning plots were also generated. The results were finally compared to the expected seismic hazard in the region.

3.1. Geometric description of the three towers

The three towers chosen for this study are illustrated by Figure 7. The first tower (Tower 1, Figure 7(a)) selected for analysis is the bell tower of San Giacomo church, found in the town of Polesine, Mantua. The tower is constructed of clay bricks, with a height of 25.5 m and dimensions of 4.6 × 4.6 m at the base, which gradually tapers to 3.8 × 3.8 m in the belfry due to the diminishing thickness of the walls — which in turn taper from 80 cm at the bottom of the structure to 40 cm near the top (Valente and Milani 2016b). The tower is freestanding, i.e. completely separated from the church, thus ruling out the possibility of any type of dynamic interaction between the two structures (Valente and Milani 2016b). Small openings are present on all four façades, with larger arched openings present in the belfry.

The second tower (Tower 2, Figure 7(b)) is a clock tower found in the town of Lendinara, Veneto. Similar to Tower 1, it is approximately square in plan and constructed entirely in brick, with a height of 25.7 m and base dimensions of 7.2 × 8.0 m (Valente and Milani 2016b). The walls are roughly 100 cm thick for the bottom 12.6 m, with this thickness reducing to 50 cm near the top (Valente and Milani 2016b). Two large arches are present on the eastern and western façades at the bottom of the structure (Valente and Milani 2016b). Unlike Tower 1, part of the northern and southern façades appear to be connected to the adjacent buildings. All four façades have large double openings at the upper level of the structure, with rampart elements present at the very top (Valente and Milani 2016b).

The third tower (Tower 3, Figure 7(c)) is the tower of Treves Castle, located in the town of Arqua Polesine, Veneto. As in the case of Towers 1 and 2, this tower is also square in plan, with base dimensions of 7.2 × 7.2 m and a height of 23.8 m (Valente and Milani 2016b). Internally the structure is subdivided into four tiers, with each tier comprising a square room with a barrel-vaulted ceiling (Valente and Milani 2016b). Wall thickness varies from tier to tier, with thicknesses of 160 cm, 120 cm, 100 cm and 80 cm on the ground, first, second and third floors respectively (Valente and Milani 2016b). Small openings in the form of windows and a door are present on the northern and southern façades, while part of the western façade is connected to the adjoining castle.

Using the above information as well as plan and elevation drawings found in Valente and Milani (2016b), 3D models were then generated in the CAD software Rhino for each of the three towers, as illustrated in Figure 7(d).

3.2. Mechanisms selected for rocking analysis

3.2.1. Tower 1

In the case of Tower 1, three different collapse mechanisms were selected for analysis, all of which involve the belfry, as illustrated by Figure 8. These mechanisms occur high enough up the structure so that amplification effects may be important. While mechanisms 1a and 1b involve corner failure, with cracks originating at the opening of the belfry, mechanism 2 is a variation of the symmetric rocking portal frame. In the case of the corner mechanisms, the crack angles were chosen to represent both an average value ($\alpha_c = 45°$, 1a) as well as an upper limit ($\alpha_c = 70°$, 1b) for a range of different brick aspect ratios and bond patterns (Malomo, DeJong, and Penna 2021).

Once the collapse mechanisms (and their corresponding axes of rotation) have been defined in Rhino, the tool then calculates the equivalent rocking parameters, which are needed to solve the corresponding equations of motion given by Equation (3). The equivalent rocking parameters for the various collapse mechanisms considered for Tower 1 are listed in Table 1.
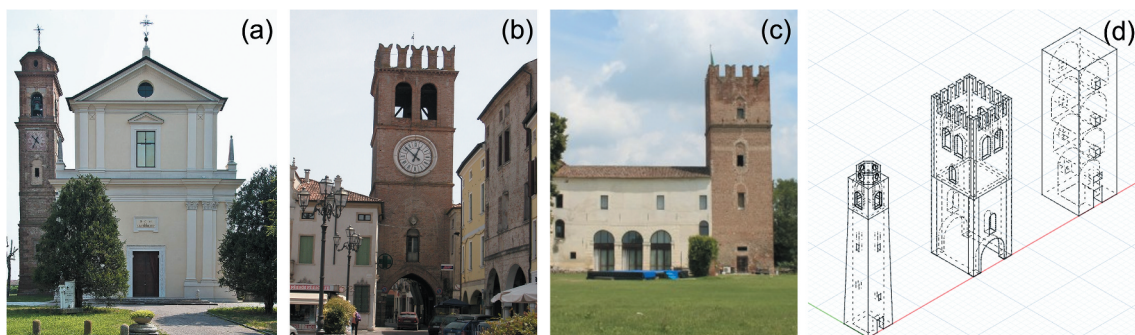

Figure 7. Towers selected for analysis: (a) Tower 1 (t1) — Bell tower of San Giacomo church (far left, Chiese Italiane), (b) Tower 2 (t2) — Clock tower in Lendinara (Wikimedia Commons), (c) Tower 3 (t3) — Tower of Treves Castle (far right, Luigi Prearo) and (d) Rhino/CAD models of the three towers.
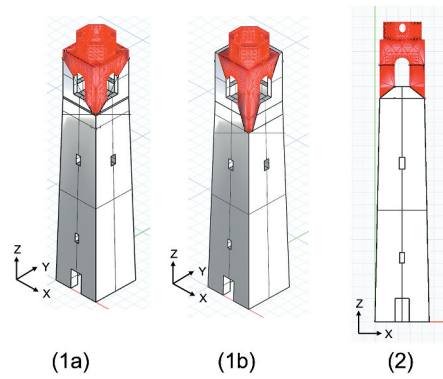
(1a)   (1b)   (2)

Figure 8. Tower 1 collapse mechanisms selected for analysis: (1a) corner failure with a crack angle $\alpha_c = 45°$, (1b) corner failure with a crack angle $\alpha_c = 70°$ and (2) symmetric portal frame mechanism.

Table 1. Equivalent rocking parameters for the different Tower 1 mechanisms.

	p_{eq} (s^{-1})	λ (rad)	ϕ_{ov} (rad)	n_s	η	h_m (m)
t1_m1a	1.33	0.49	0.49	1	−0.14	19.15
t1_m1b	1.22	0.34	0.34	1	−0.38	17.66
t1_m2	1.04	0.76	0.62	2	0.90	19.00

3.2.2. Tower 2

In the case of Tower 2, six different collapse mechanisms were selected for analysis, as illustrated by Figure 9. Mechanisms 1a and 1b arise from the development of large diagonal cracks across the structure, while mechanism 2 involves overturning of one of the rampart elements at the very top of the tower. Mechanisms 3a and 3b involve corner failure, with cracks originating at the large double openings, while mechanism 4 is a variation of the asymmetric portal frame. In the case of mechanisms 1 and 3, the crack angles were once again selected to represent both an average value ($\alpha_c = 45°$, 1a and 3a) as well as an upper limit ($\alpha_c = 70°$, 1b and 3b) for a range of different brick aspect ratios and bond patterns. The equivalent rocking parameters as computed by the tool for each of these different mechanisms can be found in Table 2.

3.2.3. Tower 3

Finally, in the case of Tower 3, four different collapse mechanisms were selected for analysis as illustrated by Figure 10. All considered mechanisms are variations of single block overturning failure, with the mechanisms developing due to large diagonal cracks originating at one or more of the window openings. As in the case of Towers 1 and 2, the crack angles were selected to represent both an average value ($\alpha_c = 45°$, 1a/b) as well as an upper limit ($\alpha_c = 70°$, 1c/d) to account for uncertainties associated with the brick aspect ratio and bond pattern.

Table 3 lists the equivalent rocking parameters computed by the tool for these different mechanisms.

3.3. Modal analyses

As all considered mechanisms take place above ground level ($h_m > 0$), finite element models of the three towers were automatically generated by the tool and modal analyses were conducted. The results of these analyses were used to transform the structures into equivalent single-degree-of-freedom (SDF) elastic oscillators — which in turn were used to account for the amplification and filtering of the ground motion by the structures in a simplified manner. The material properties assumed for all models were that of an elastic isotropic material characterised by a Young's modulus $E = 0.84$ GPa, a Poisson's ratio $\nu = 0.2$ and density $\rho = 2000$ kg/m^3. Note that these values were calibrated based on the first two modal frequencies obtained for each of the towers from the literature (Valente and Milani 2016b).

As Tower 1 is freestanding, only one FE model of the structure needed to be generated. However, in the case of Tower 2, the bottom 8.55 m of the structure is connected to adjacent buildings on the northern and southern façades, with limited information available about the type/level of connectivity. Therefore, two different boundary conditions were considered to provide a lower and upper bound of the response. These are the isolated case (zero connectivity to the adjacent
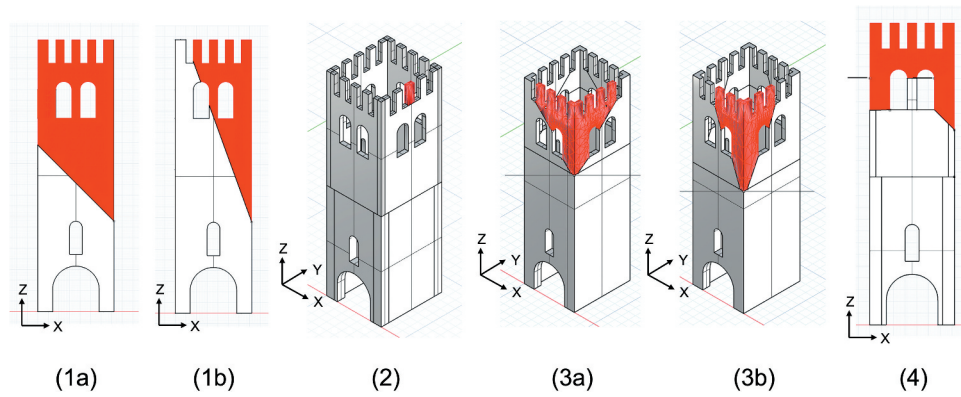
Figure 9. Tower 2 collapse mechanisms selected for analysis: (1a) overturning failure with a crack angle $a_c = 45°$, (1b) overturning failure with a crack angle $a_c = 70°$, (2) single-block rampart overturning, (3a) corner failure with a crack angle $a_c = 45°$, (3b) corner failure with a crack angle $a_c = 70°$ and (4) asymmetric portal frame mechanism.

Table 2. Equivalent rocking parameters for the different Tower 2 mechanisms.

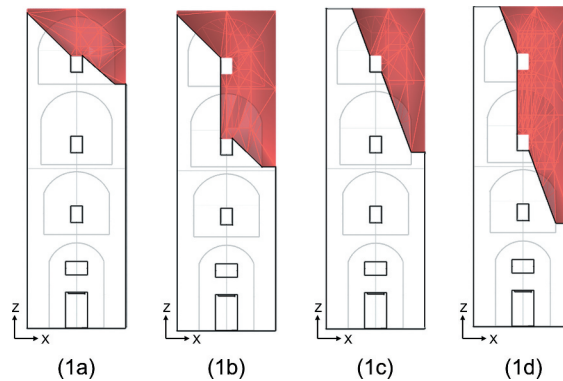|	p_{eq} (s^{-1})	λ (rad)	ϕ_{ov} (rad)	n_s	η	h_m (m)
t2_m1a	0.89	0.30	0.30	1	−0.27	8.55
t2_m1b	0.92	0.11	0.11	1	−0.50	8.55
t2_m2	2.55	0.22	0.22	2	0.93	23.50
t2_m3a	1.22	0.33	0.33	1	−0.35	17.10
t2_m3b	1.12	0.20	0.20	1	−0.56	15.00
t2_m4 (+)	0.91	0.60	0.55	2	0.90	16.60
t2_m4 (-)	1.01	0.96	0.61	2	0.90	18.30

Figure 10. Tower 3 collapse mechanisms selected for analysis. Overturning failure with: (1a) cracks originating at the first window with crack angles $a_c = 45°$, (1b) cracks originating at the first and second windows with crack angles $a_c = 45°$, (1c) cracks originating at the first window with crack angles $a_c = 70°$ and (1d) cracks originating at the first and second windows with crack angles $a_c = 70°$.

Table 3. Equivalent rocking parameters for the different Tower 3 mechanisms.

	p_{eq} (s^{-1})	λ (rad)	ϕ_{ov} (rad)	n_s	η	h_m (m)
t3_m1a	1.27	0.56	0.56	1	−0.03	18.20
t3_m1b	1.02	0.28	0.28	1	−0.34	12.20
t3_m1c	1.09	0.21	0.21	1	−0.43	13.13
t3_m1d	0.92	0.16	0.16	1	−0.47	7.68

structures) and the fixed case (tower completely restrained, i.e. pinned, to the adjacent structures). Similarly in the case of Tower 3, the bottom 11.2 m of its western façade is connected to the adjacent castle, but again with limited information available about the connection quality. Both isolated and fixed case models were considered for this tower as well. The results of the modal analyses can be found in Figure 11.

3.4. Full time-history analyses

Full time-history analyses were subsequently conducted to gauge the response of the structures/mechanisms to a suite of earthquake ground motions. Using the PEER NGA-West2 ground motion database (PEER 2014), 15 different ground motions (comprising a mix of pulse and non-pulse type records) were selected for analysis, scaled to the site-specific response spectrum as defined in Eurocode 8 (EN 1998–1 2004) assuming soil type C — and as illustrated by Figure 12. Incremental dynamic analyses (IDA) were then conducted for different levels of scaling of the earthquake ground motions to capture the behaviour of each mechanism from small rotations all the way up to collapse. The intensity measure (IM) selected for the IDA curves was the PGA of the target spectrum, while the structural response (engineering design parameter) was expressed in terms of the maximum predicted rotation ϕ_{max} normalised by the overturning rotation ϕ_{ov}. As all three towers are located in a zone of low/medium seismicity, with a maximum PGA of 0.10–0.175 g expected with a 2% probability of exceedance in 50 years (OPCM 2006), the ground motion applied to the towers was consequently scaled starting from a PGA of 0.01 g all the way up to 0.70 g (in steps of 0.02 g) to gauge the vulnerability of the structures to collapse for different factors of safety.

Equation (5) was consequently solved for the two SDF elastic oscillators (for the fundamental modes of the isolated and fixed cases respectively) for each of the ground motions for each PGA, and the response scaled to get the final input signals at the base of the rocking mechanisms. The filtered and scaled input signals were then substituted into Equation (3), which was solved to predict the response of each of the rocking mechanisms to the different ground motions, for both the isolated and fixed cases, with the predictions expressed in terms of rotation ϕ over time. For each mechanism, the median maximum response was compared for the different levels of scaling of the ground motion suite, for both connectivity cases (i.e. isolated and fixed).

3.5. Pulse response

In addition to capturing the evolution of the dynamic behaviour of the structures from small rotations to collapse, incremental dynamic analyses can also provide an indication of the relative vulnerability of the different collapse mechanisms. However, they can be computationally expensive and time-consuming to generate. Overturning plots, on the other hand, represent an efficient alternative to such analyses, particularly in the case of near-source ground motions.
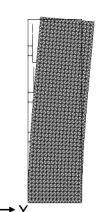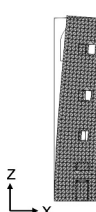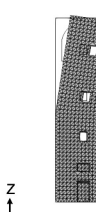
Figure 11. Fundamental frequencies of the three towers for the different boundary conditions.

Figure 12. Elastic acceleration spectra (normalised by PGA) of the ground motions selected for analysis. Note that the site-specific target spectrum is shown with a black solid line, while the mean spectrum is shown in red.

Thus, pulse response analyses were also conducted to compare the different mechanisms in a more rapid manner. To that end, overturning plots were g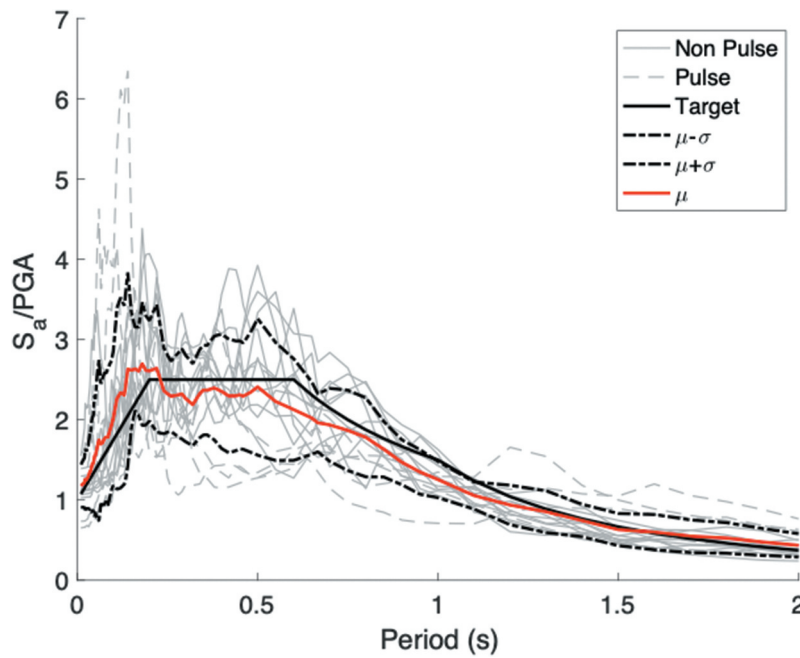enerated following the approach outlined in Section 2.5 for the different mechanisms of each tower, using as input the kinematic constants as calculated in Section 3.2 as well as the fundamental frequencies and corresponding mode shapes for the different towers (for both the isolated and fixed cases) as determined from the modal analyses in Section 3.3.

4. Results

4.1. Tower 1

For each collapse mechanism for Tower 1, the maximum predicted rotation ϕ_{max} (normalised by the overturning rotation ϕ_{ov}) was compared for each of the different ground motion records. This comparison was conducted for the different levels of scaling of the ground motion suite, ranging from a PGA = 0.20 g (for rocking to initiate for all the mechanisms) to 0.70 g (to cause collapse), as illustrated by Figure 13. Additionally, to compare the relative vulnerabilities of the different mechanisms more easily, the median maximum response of each mechanism was plotted (in red) as well.

As Figure 13 illustrates, mechanism t1_m1b appears to be the most vulnerable to collapse — due in part to being the most slender — consistently experiencing the

largest rotations and overturning for the lowest level of scaling of the ground motion (0.48 g for the median case). Note that overturning in this paper is defined as taking place when $\phi_{max}/\phi_{ov} = 1$, although failure would occur at lower rotations in reality. Conversely mechanism t1_m2 displays the highest resistance to collapse, experiencing a median maximum rotation of only 0.21 ϕ_{max}/ϕ_{ov} for the highest level of scaling of the ground motion suite.

These observations are also corroborated by the overturning plots generated for these mechanisms. As Figure 14 demonstrates, for the given range of pulse frequencies, mechanism t1_m1b will overturn for the lowest pulse amplitudes, while mechanism t1_m2, due to its relatively stocky nature, requires the highest pulse amplitudes to collapse.

4.2. Tower 2

For Tower 2, the first set of full time-history (IDA) analyses were conducted on mechanisms t2_m1a and t2_m1b, for both the isolated and fixed cases, to better understand the influence of different boundary conditions on dynamic response. As in the case of Tower 1, the ground motion suite was once again scaled from a PGA = 0.20 g (for rocking to initiate) to 0.70 g. As Figure 15 illustrates, the isolated case of mechanism t2_m1b displays the highest vulnerability to collapse; overturning is predicted for the lowest level of ground motion scaling (PGA = 0.28 g for the median case,
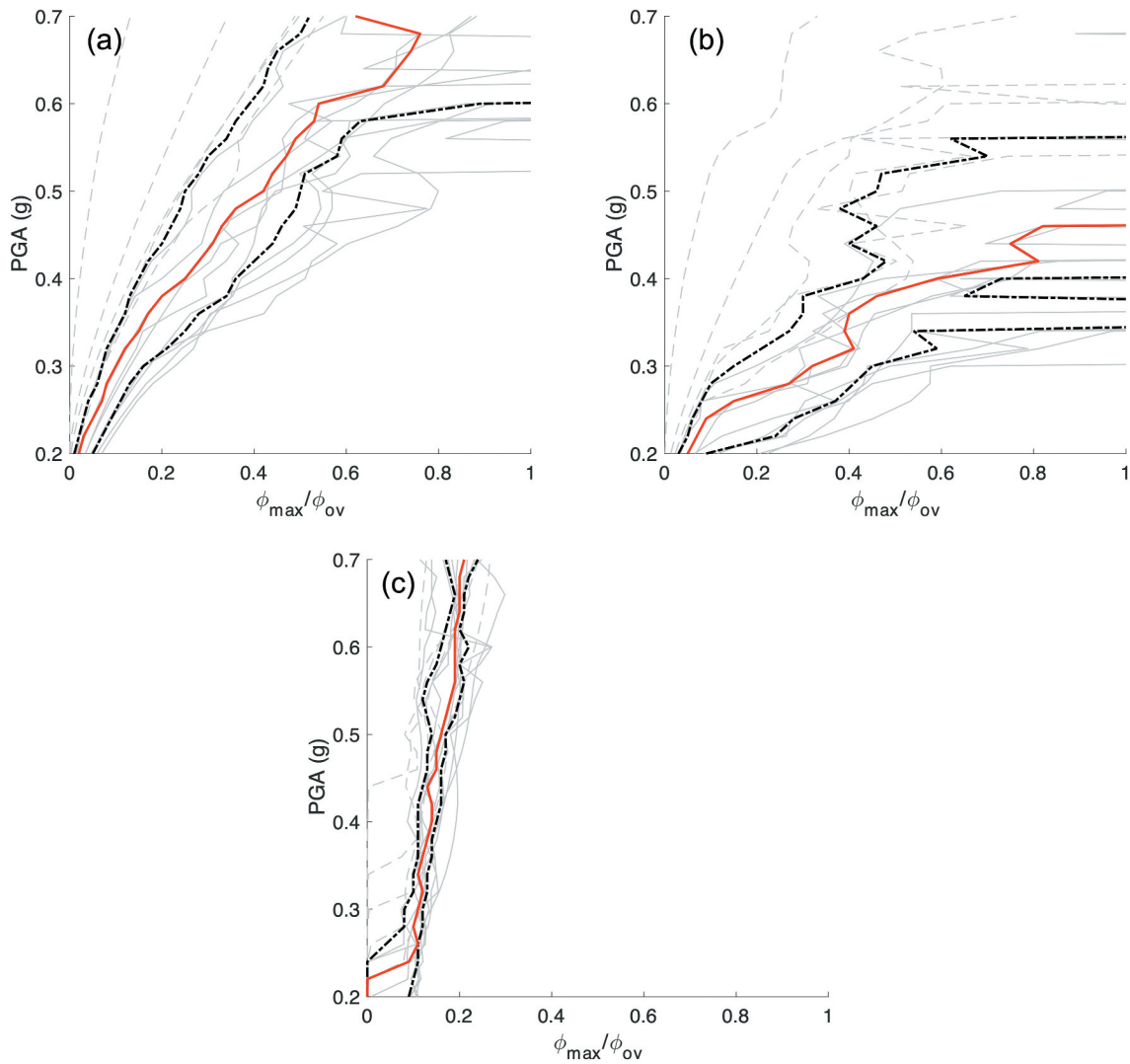
Figure 13. IDA curves for Tower 1 mechanisms: (a) t1_m1a, (b) t1_m1b and (c) t1_m2. Median values shown in red, first and third quartiles in black, and response to each ground motion record indicated in grey.
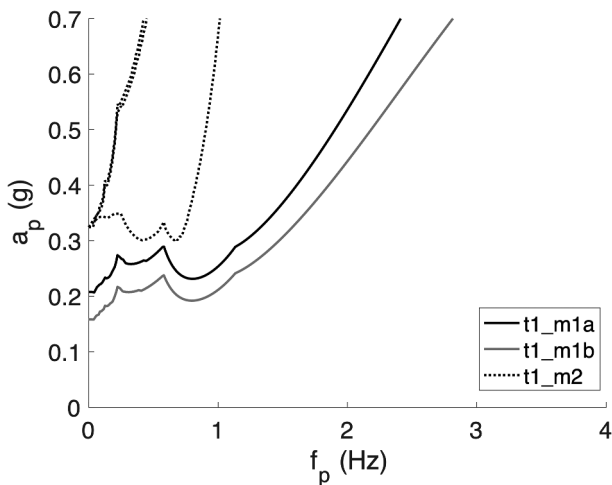

Figure 14. Scaled overturning plots generated for the different Tower 1 mechanisms.

although resurrections typical of the rocking response (Lachanas and Vamvatsikos 2022) were also observed to occur for 0.30 g). Meanwhile, the IDA curve for the fixed case of t2_m1b displays comparable behaviour to that of the isolated case of t2_m1a — indicating that the benefits of fixing the boundary conditions for t2_m1b are akin to decreasing the slenderness of the mechanism (from $\lambda = 0.11$ to $\lambda = 0.30$). The fixed case of t2_m1a, on the other hand, records the smallest — almost imperceptible — rotations, recording a median maximum rotation of $\phi_{max}/\phi_{ov} = 0.02$ for the highest level of ground motion scaling.

In the case of mechanism t2_m2, analyses were again conducted using both the isolated and fixed case models. However, in this case the ground motion suite was scaled from a PGA = 0.01 g to 0.25 g, in order to capture the range of the actual maximum PGA expected on site
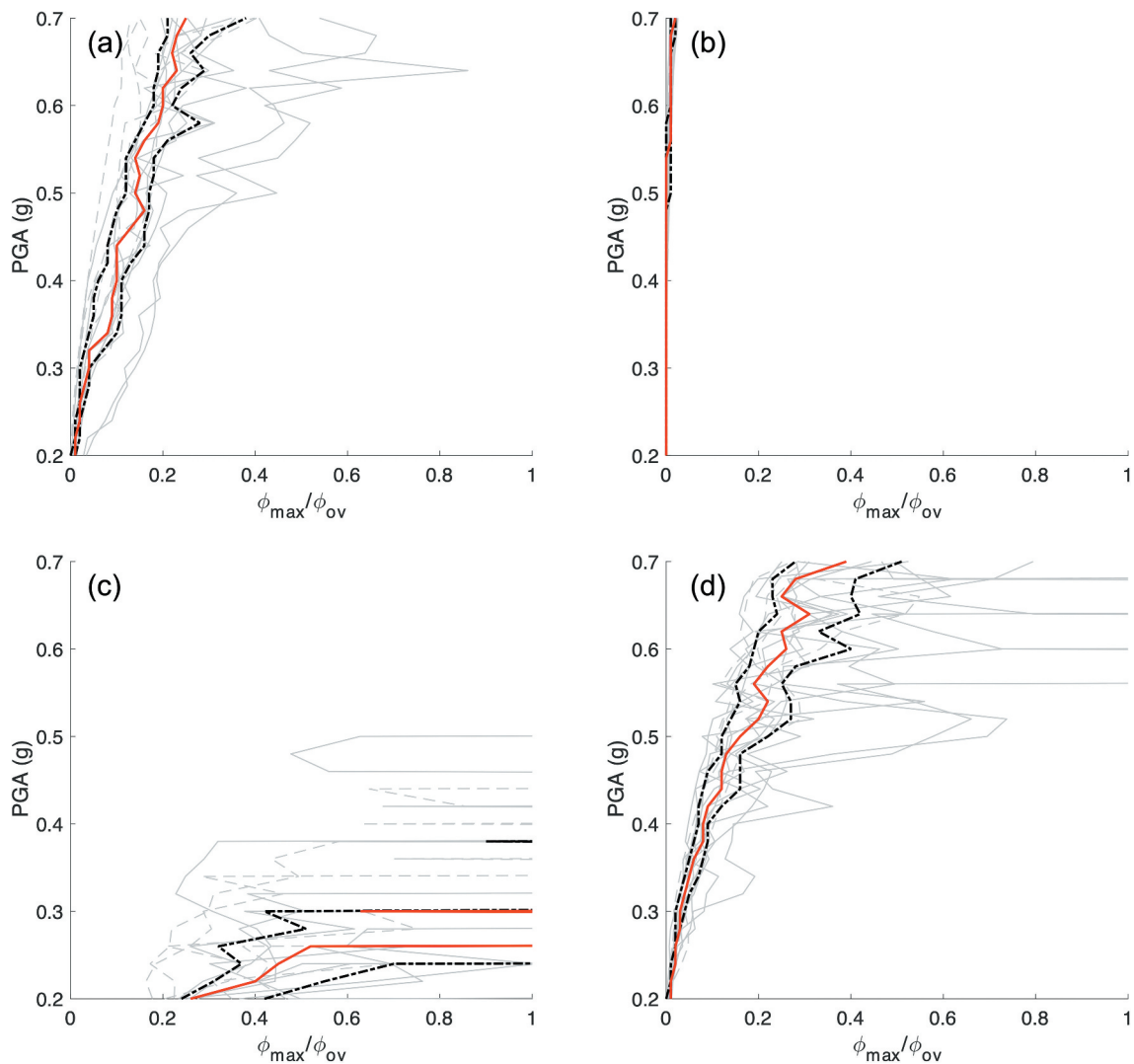
Figure 15. IDA curves for Tower 2 mechanisms: (a) t2_m1a isolated, (b) t2_m1a fixed, (c) t2_m1b isolated and (d) t2_m1b fixed cases. Median values shown in red, first and third quartiles in black, and response to each ground motion record indicated in grey.

(OPCM 2006). As Figure 16 illustrates, the isolated case fails via overturning for a relatively low level of scaling of the earthquake ground motion (0.12 g for the median case). Note that this is within the range of the 0.10–0.125 g PGA expected on site for the case of 2% probability of exceedance in 50 years. By comparison, the fixed case predictably displays a higher resistance to collapse, with failure via overturning only occurring for one of the records for this same level of ground motion scaling.

The next set of analyses were conducted on mechanisms t2_m3a and t2_m3b, where the ground motion suite was again scaled from a PGA = 0.20 g (to initiate rocking for the stockier mechanism t2_m3a) to 0.70 g. The results of these analyses are presented in Figure 17 for both the isolated and fixed cases. As Figure 17 illustrates, the isolated case of mechanism t2_m3b displays the highest vulnerability to collapse, overturning for the

lowest level of ground motion scaling (0.28 g for the median case). By comparison, the isolated case of mechanism t2_m3a only overturns for a PGA of 0.46 g and above (for the median case). It is clear that in this case the slenderness of t2_m3b (λ = 0.20, as opposed to λ = 0.33 for t2_m3a) controls the response, resulting in overturning of t2_m3b more frequently and for a lower PGA than t2_m3a, despite the fact that both mechanisms are of similar scale; t2_m3a also occurs slightly higher up than t2_m3b and consequently experiences a greater degree of amplification. Similarly, for the fixed case, t2_m3a displays a higher resistance to collapse than t2_m3b. As in the case of the previously considered mechanisms for this tower, the predictions for the fixed case are also considerably less conservative than their isolated counterparts.

The final set of analyses for Tower 2 were conducted on mechanism t2_m4 (the asymmetric portal frame). Due

Figure 16. IDA curves for Tower 2 mechanism 2: (a) isolated and (b) fixed cases. Median values shown in red, first and third quartiles in black, and response to each ground motion record indicated in grey.
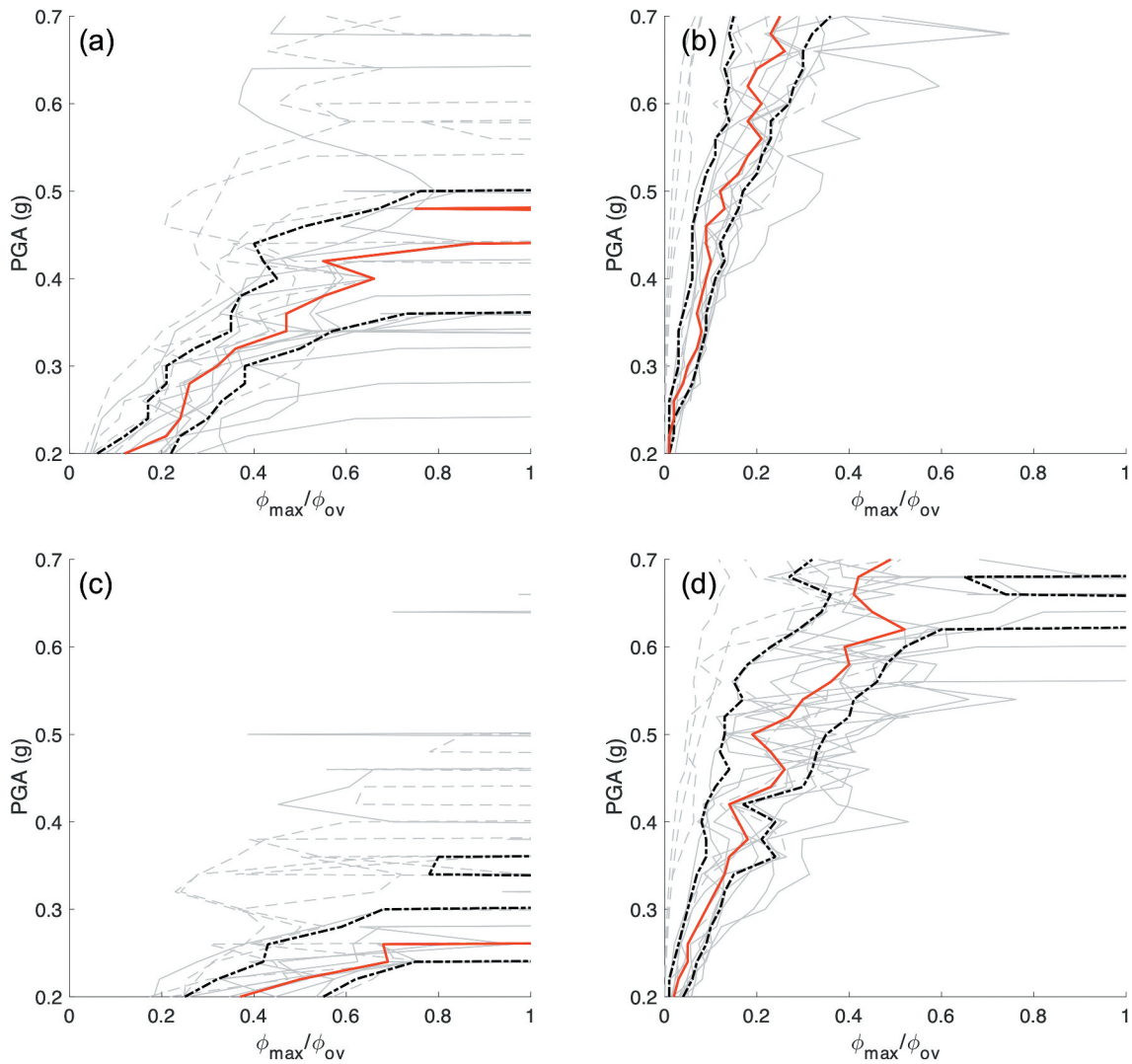
Figure 17. IDA curves for Tower 2 mechanisms: (a) t2_m3a isolated, (b) t2_m3a fixed, (c) t2_m3b isolated and (d) t2_m3b fixed cases. Median values shown in red, first and third quartiles in black, and response to each ground motion record indicated in grey.

to the relatively stocky nature of this mechanism, the ground motion was again scaled from a PGA = 0.20 g (for rocking to initiate) to 0.70 g. As Figure 18 illustrates, the fixed case again displays a higher resistance to collapse than the isolated case, however overturning was not found to occur for either case.

Overturning plots were also generated to more directly compare the relative vulnerabilities of the different mechanisms, for both the isolated (Figure 19(a)) and fixed (Figure 19(b)) cases. As Figure 19 demonstrates, mechanism t2_m2 displays the highest vulnerability to collapse for both cases. Additionally for the isolated case, mechanisms t2_m1b and t2_m3b display similar vulnerabilities to collapse — despite mechanism t2_m1b being nearly twice as slender as t2_m3b ($\lambda = 0.11$ vs $\lambda = 0.20$). This is at least in part due to the fact that t2_m3b occurs about 75% higher up the tower than t2_m1b, and thus experiences a higher level of amplification which counteracts the effect of the slenderness. Conversely, for the fixed case, the slenderness of t2_m1b appears to dominate for pulse frequencies less than 1.5 Hz. For higher pulse frequencies, mechanisms

t2_m3b and then t2_m3a appear to display a higher vulnerability to collapse, albeit for much higher levels of scaling of the pulse amplitude. For both the isolated and fixed cases, mechanism t2_m4 displays the highest resistance to collapse due to its relatively stocky nature. As in the case of the IDA curves, the fixed case models appear to yield much more conservative predictions than their isolated counterparts.

4.3. Tower 3

In the case of Tower 3, all four collapse mechanisms were assessed simultaneously, with the results presented for both the isolated and fixed cases (Figure 20). The ground motion was again scaled from a PGA = 0.20 g (for rocking to initiate for all four mechanisms) to 0.70 g.

As Figure 20 illustrates, if the tower is assumed to be freestanding (i.e. isolated), failure is most likely to occur via mechanism t3_m1c — with this mechanism exhibiting the largest rotations and overturning for a PGA = 0.58 g (for the median case). Note that for
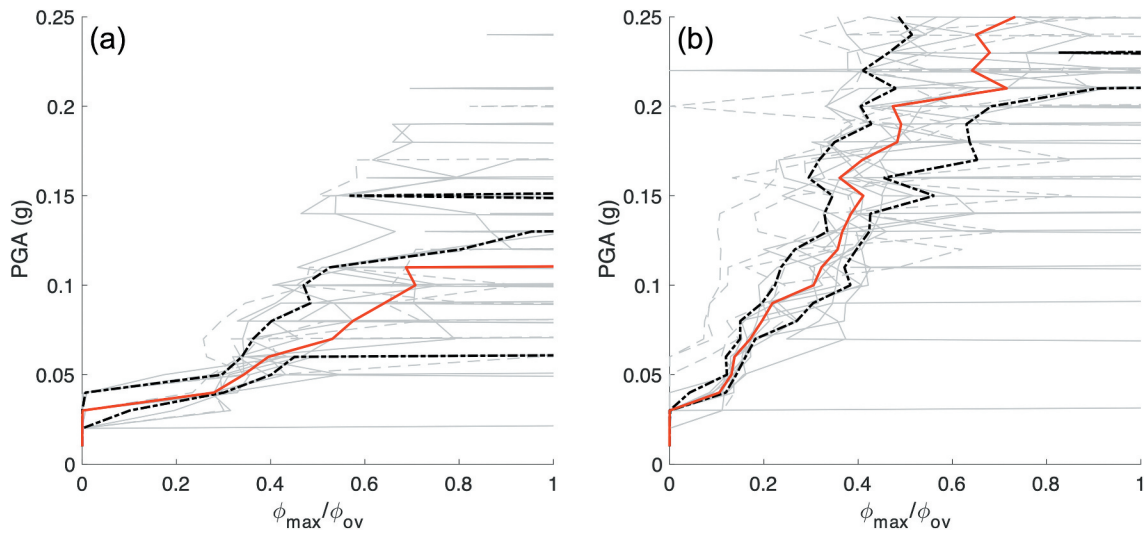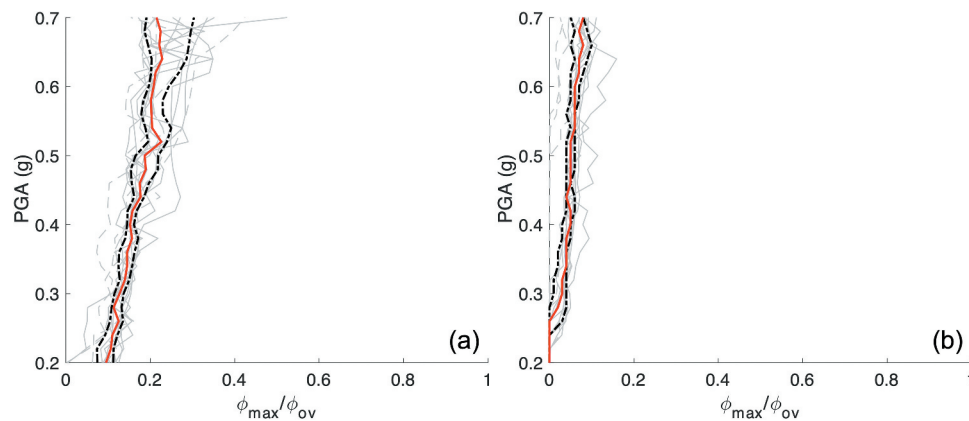

Figure 18. IDA curves for Tower 2 mechanism 4: (a) isolated and (b) fixed cases. Median values shown in red, first and third quartiles in black, and response to each ground motion record indicated in grey.


Figure 19. Scaled overturning plots generated for the different Tower 2 mechanisms for both the (a) isolated and (b) fixed cases.

Figure 20. IDA curves for Tower 3 mechanisms: (a) t3_m1a isolated and (b) fixed, (c) t3_m1b isolated and (d) fixed, (e) t3_m1c isolated and (f) fixed and (g) t3_m1d isolated and (h) fixed. Median values shown in red, first and third quartiles in black, and response to each ground motion record indicated in grey.
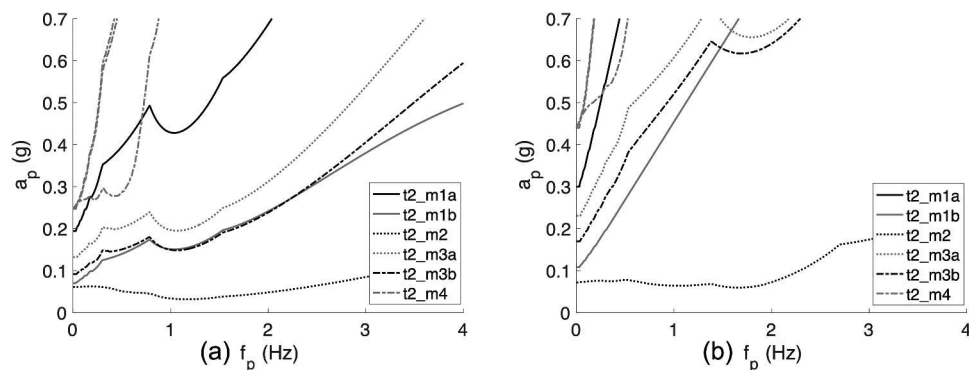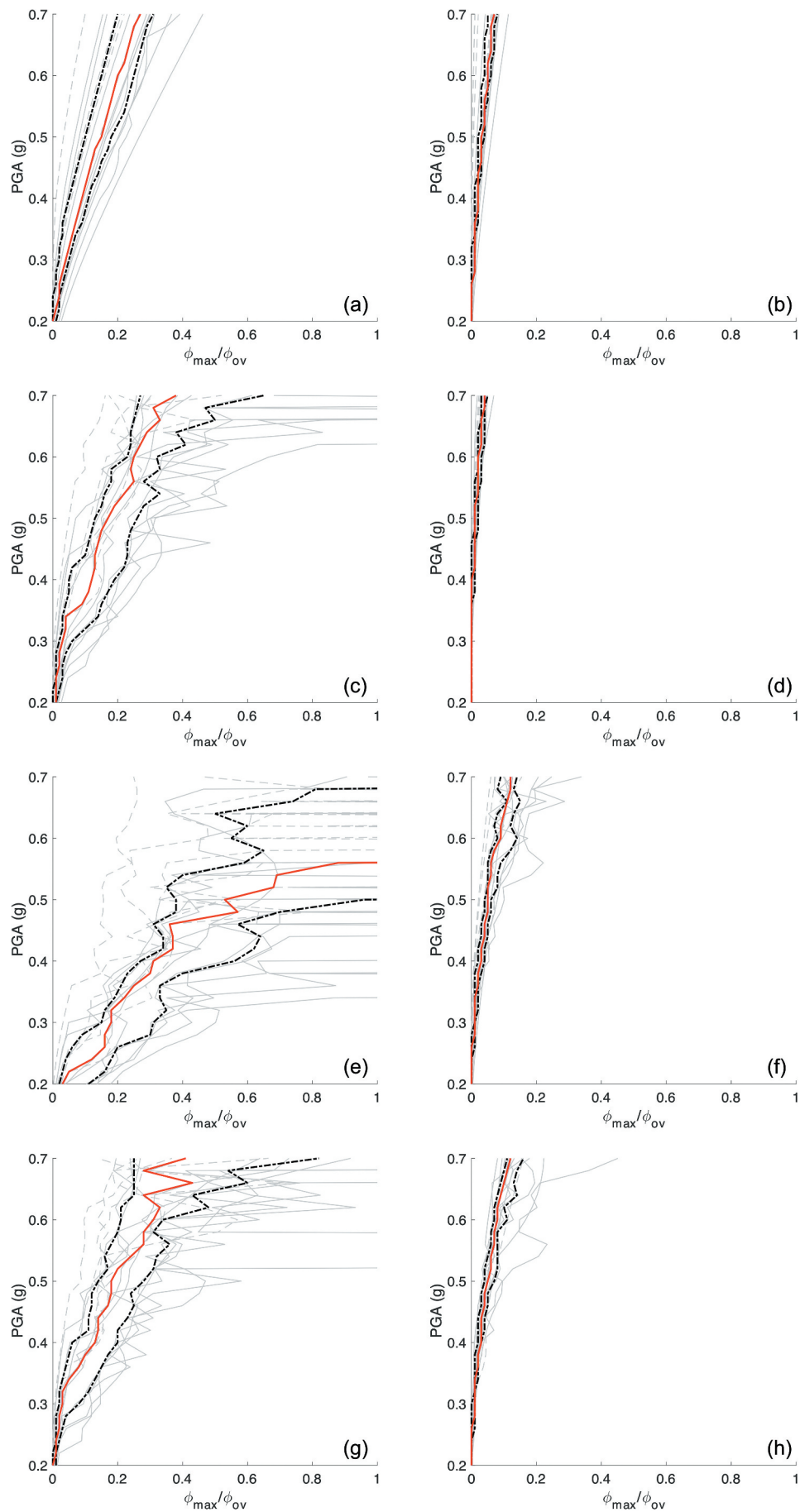
this same level of scaling of the ground motion suite, median ϕ_{max}/ϕ_{ov} values of only 0.19, 0.24 and 0.28 were recorded for mechanisms t3_m1a, t3_m1b and t3_m1d respectively. The similarities in response for mechanisms t3_m1a and t3_m1b, in particular, could be attributed to the trade-off between amplification and mechanism slenderness. While t3_m1a (λ = 0.56) takes place at a height of 18.20 m and experiences an average maximum acceleration of 1.78 g at its base (using as an example here a PGA scaling of 0.50 g), it undergoes rotations of a similar magnitude to t3_m1b (λ = 0.28), which is twice as slender but experiences slightly more than half the maximum base acceleration (0.93 g).

If the tower is assumed to be fixed to the adjacent castle, the resulting IDA curves for mechanisms t3_m1a and t3_m1b are again similar, as are the curves for t3_m1c and t3_m1d. However, for all four mechanisms relatively small responses are recorded, with median maximum rotations in range of 0.04 to 0.12 ϕ_{max}/ϕ_{ov}. It is interesting to note that in the case of mechanism t3_m1d, despite the isolated and fixed models both experiencing similar average maximum accelerations at their bases, the fixed case model records median ϕ_{max}/ϕ_{ov} values that are, on average, almost a third of the values recorded by its isolated counterpart.

These observations are corroborated by the overturning plots generated for these mechanisms as illustrated by Figure 21(a) (for the isolated case) and Figure 21(b) (for the fixed case). As Figure 21(a) illustrates, mechanism t3_m1c is the most vulnerable to collapse for all considered pulse frequencies for the isolated case, while mechanisms t3_m1a and t3_m1b display similar vulnerabilities to failure. However, in terms of relative vulnerabilities, mechanism t3_m1d appears to be the second-most vulnerable to collapse for pulse frequencies less than 0.8 Hz and greater than 1.9 Hz, while for the intermediate frequencies mechanisms t3_m1a and t3_m1b are more vulnerable. Conversely for the fixed case (Figure 21(b)), mechanism t3_m1d consistently

displays the highest vulnerability to failure, closely followed by mechanism t3_m1c, while mechanisms t3_m1a and t3_m1b again display similar vulnerabilities to collapse.

5. Discussion

5.1. Importance of accounting for amplification effects

To demonstrate the importance of accounting for amplification effects, the median IDA curves for Tower 2 mechanism 4 were compared for the isolated, fixed and no amplification cases. As Figure 22 illustrates, for the considered range of ground motion scaling, the isolated model experiences the largest rotations, with a maximum median response of 0.23 ϕ_{max}/ϕ_{ov}, which reduces to 0.08 ϕ_{max}/ϕ_{ov} for the fixed case. Neglecting amplification effects entirely, on the other hand, results in rocking not initiating for a majority of the ground motions until the suite is scaled to a PGA of 0.54 g, and resulting in a median maximum response of 0.0009 ϕ_{max}/ϕ_{ov} for the highest level of scaling of 0.70 g. Note that this is only 0.4% and 1.1% of the corresponding responses obtained for the isolated and fixed cases respectively, thus underscoring just how unconservative this assumption can be — especially when analysing the behaviour of tall slender masonry structures.

5.2. Influence of boundary conditions on dynamic response

As the previous section demonstrates, the models with fixed boundary conditions consistently appear to record smaller displacements than their isolated counterparts. This is due in part to the extent of amplification experienced by the ground motion, which depends in turn on the frequency of the structure. As Figures 11 and 23
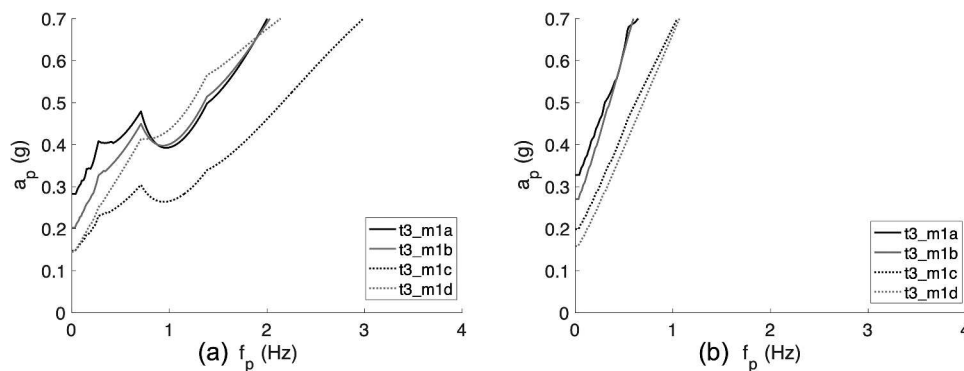

Figure 21. Scaled overturning plots generated for the different Tower 3 mechanisms for both the (a) isolated and (b) fixed cases.
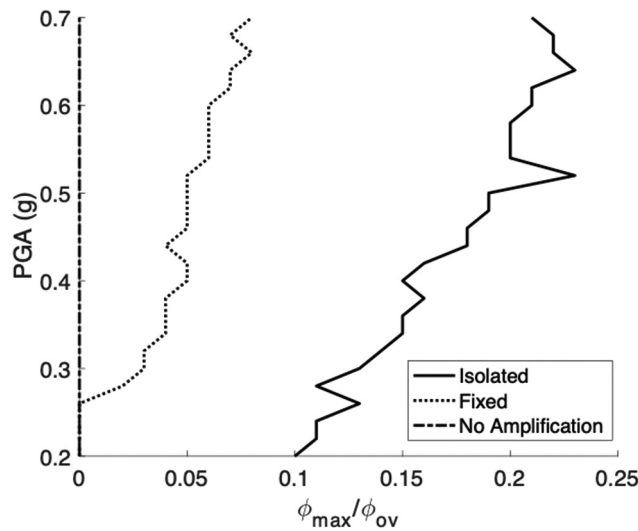
Figure 22. Comparison of Tower 2 Mechanism 4 median responses for isolated, fixed and no amplification cases.

illustrate, the towers with isolated boundary conditions have lower fundamental frequencies (longer periods) than their fixed counterparts. In the case of the three towers considered in this paper, this generally results in a lower initial elastic amplification (Figure 23(a)). However, the initial response is computed at the effective modal height h_e which then needs to be scaled to the mechanism height h_m using the ratio $u(h_m)/u(h_e)$ as extracted from the mode shape (shown here in Figure 23(b) for Tower 2). For most mechanisms considered in this study, this ratio is generally larger for the isolated case than the fixed case, resulting in a greater

magnitude of acceleration being experienced at the base of the isolated case mechanisms.

Furthermore, the isolated and fixed boundary conditions also influence the frequency at which the structure responds to the initial input ground motion — with the filtered accelerations experienced at the base of the rocking mechanisms having a frequency content similar to that of the fundamental frequency of the structure. As the isolated case generally has a lower frequency than its fixed counterpart, its filtered ground motion is consequently more destructive for the rocking mechanism. This is one explanation for why in the case of
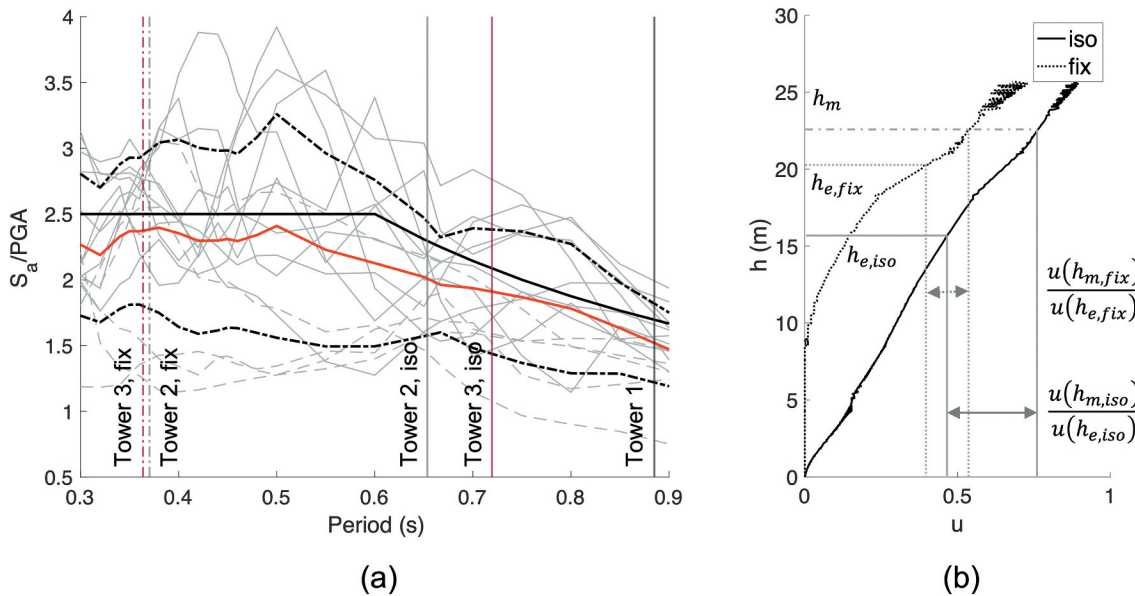

Figure 23. Influence of boundary conditions on: (a) initial elastic amplification of the ground motion and (b) variation of amplification with height for Tower 2 (mode shape).

mechanism t3_m1d, despite similar magnitudes of acceleration being experienced at the base of the mechanism, the isolated model results in rotations that are three times as large as those of the fixed model.

5.3. Full time-history analyses vs pulse response

In general, a fairly good agreement was observed between the full time-history analyses (IDA) and the overturning plots with respect to the relative vulnerabilities of the different mechanisms. While full time-history analyses make it possible to predict the maximum response of the structures for different levels of scaling of the earthquake ground motion, they have a high associated computational cost. Overturning plots, on the other hand, enable rapid comparison of the different collapse mechanisms — however they can only predict whether or not a given sinusoidal pulse (characterised by a certain frequency and amplitude) will cause the structure to collapse, and thus do not provide insight on the maximum response of the structure to a specific hazard scenario. However, in the absence of representative ground motions, and until ground motion prediction methods shift to focus on expected pulse magnitudes, such plots represent a viable alternative to compare the relative dynamic resilience of the different collapse mechanisms.

5.4. Practical implications

To determine the actual vulnerability of the various mechanisms considered in this study to collapse, the median ϕ_{max}/ϕ_{ov} values for each of the mechanisms were compared for the isolated case, with the ground

motion suite scaled to the maximum PGA expected on site. This corresponds to a PGA of 0.175 g for Tower 1 and 0.125 g for Towers 2 and 3, assuming 2% probability of exceedance in 50 years. In this case, only mechanism t2_m2 (the single-block rampart mechanism) was found to be in danger of failure via overturning collapse. The next two largest responses were of mechanisms t2_m3b (corner failure, $\alpha_c = 70°$) and t2_m1b (single block with a large diagonal crack, $\alpha_c = 70°$), although they are significantly smaller than those of t2_m2, with median ϕ_{max}/ϕ_{ov} values of 0.15 and 0.13 respectively. These responses are, however, close to the allowable rotation specified by the Italian building code (which for the assessment of overturning corresponds to 40% of 0.4 $\phi_{max}/\phi_{ov} = 0.16$) (DMI 2008). Note that all the other mechanisms recorded much smaller responses, in the range of 0.00 (i.e. no rocking or imperceptible rotations) to 0.03 ϕ_{max}/ϕ_{ov}.

Thus to better exemplify how this procedure could be applied to the assessment of such structures, the median ϕ_{max}/ϕ_{ov} values for each of the mechanisms were again compared for the isolated models, but now for the case where the ground motion suite was scaled to a PGA of 0.3 g — as illustrated by Figure 24. This comparison makes it possible to determine the relative vulnerabilities of the different mechanisms to collapse and consequently prioritise intervention measures. As Figure 24 illustrates, for this level of scaling of the earthquake ground motion, mechanism t2_m3b was also found to be in danger of overturning failure, while the next-largest rotations (in order of decreasing magnitude) were recorded by mechanisms t2_m1b, t2_m3a (corner failure, $\alpha_c = 45°$), t1_m1b (corner failure, $\alpha_c = 70°$), and t3_m1c (cracks originating at the first window of Tower

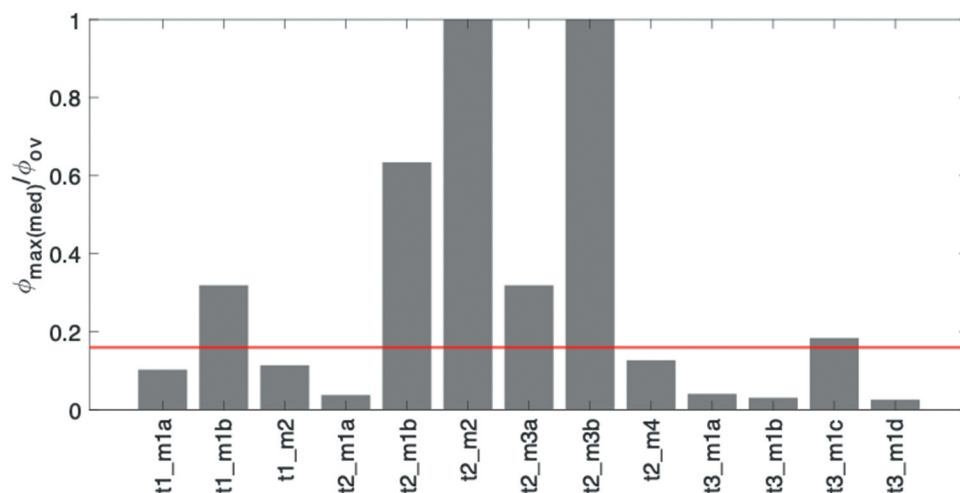**Figure 24.** Comparison of the median maximum rotations $\phi_{max(med)}$ normalised by the overturning rotation ϕ_{ov} for all considered mechanisms (isolated cases only), for ground motion that has been scaled to a PGA = 0.3 g.

3 with crack angles $\alpha_c = 70°$). Note that median maximum rotations recorded by these four mechanisms were also found to exceed the allowable rotation specified by the Italian building code ($\phi_{max}/\phi_{ov} = 0.16$, indicated by the solid red line in Figure 24).

6. Conclusions

In this paper, a new modelling strategy for the seismic collapse assessment of masonry structures is presented, which integrates finite element analysis with rocking dynamics to model the dynamic response of complex structural geometries in a computationally efficient manner. This new modelling strategy was implemented using the open-source COMPAS framework, and is exemplified through the seismic evaluation of three historic masonry towers in north-eastern Italy.

Through a series of full time-history analyses (IDA) conducted using a suite of different earthquake ground motions, and through the generation of overturning plots, it was found that elastic amplification effects can be extremely important for tall and slender masonry structures. Further, it was demonstrated that the choice of boundary conditions (isolated vs fixed) can have a substantial effect on the dynamic response — both in terms of the extent of amplification as well as the frequency content of the filtered records, which in turn influenced the rocking response of the assumed mechanisms. The predictions of ground motion pulse overturning plots were compared to full time-history analysis results, and it was found that the relative vulnerabilities predicted by these two methods were in good agreement, indicating that both methods may be useful for prioritising retrofit alternatives. However, time history analyses obviously provide more useful information for seismic assessment based on current code-based procedures that rely on elastic design spectra to quantify the hazard. Finally, it was concluded that for the level of seismic hazard expected on site, only one of the towers is in danger of local minor collapse via overturning of one of its rampart elements, while two other mechanisms within the same tower (namely corner failure and overturning via the development of a large diagonal crack across the structure) were also found to experience rotations close to the allowable rotation specified by the Italian building code for the assessment of overturning collapse.

ORCID

Anjali Mehrotra http://orcid.org/0000-0002-3453-2879
Matthew J. DeJong http://orcid.org/0000-0002-6195-839X

References

Allen, R. H., and X. Duan. 1995. Effects of linearizing on rocking-block toppling. *Journal of Structural Engineering* 121 (7):1146–49. doi:10.1061/(asce)0733-9445(1995) 121:7(1146).

Allen, R. H., I. J. Oppenheim, A. R. Parker, and J. Bielak. 1986. On the dynamic response of rigid body assemblies. *Earthquake Engineering & Structural Dynamics* 14 (6):861–76. doi:10.1002/eqe.4290140604.

Al Shawa, O., G. de Felice, A. Mauro, and L. Sorrentino. 2012. Out-of-plane seismic behaviour of rocking masonry walls. *Earthquake Engineering & Structural Dynamics* 41 (5):949–68. doi:10.1002/eqe.

American Society of Civil Engineers (ASCE). 2007. Seismic design criteria for structures, systems, and components in nuclear facilities. 43–45.

Azevedo, J., G. E. Sincraian, and J. V. Lemos. 2000. Seismic Behaviour of Blocky Masonry Structures. *Earthquake Spectra* 16 (2):337–65. doi:10.1193/1.1586116.

Castellazzi, G., A. M. D'Altri, S. de Miranda, A. Chiozzi, and A. Tralli. 2018. Numerical insights on the seismic behavior of a nonisolated historical masonry tower. *Bulletin of Earthquake Engineering* 16 (2):933–61. doi:10.1007/s10518-017-0231-6.

Clemente, P. 1998. Introduction to the dynamics of stone arches. *International Journal of Earthquake Engineering and Structural Dynamics* 27 (5):513–22. doi:10.1002/(SICI) 1096-9845(199805)27:5<513::AID-EQE740>3.0.CO;2-O.

Clementi, F., G. Milani, A. Ferrante, M. Valente, and S. Lenci. 2020. Crumbling of amatrice clock tower during 2016 central Italy seismic sequence: Advanced numerical insights. *Frattura Ed Integrita Strutturale* 14 (51):313–35. doi:10. 3221/IGF-ESIS.51.24.

D'Ayala, D., and E. Speranza. 2002. An integrated procedure for the assessment of seismic vulnerability of historic buildings. *Proceedings of the 12th European Conference on Earthquake Engineering*, London, UK, Paper 561.

DeJong, M. J. 2012. Seismic response of stone masonry spires: Analytical modeling. *Engineering Structures* 40:556–65. doi:10.1016/j.engstruct.2012.03.010.

DeJong, M. J. 2014. Rocking of structures during Earthquakes: From collapse of masonry to modern design. *SECED Newsletter* 25 (3):1–8.

DeJong, M. J., L. De Lorenzis, S. Adams, and J. A. Ochsendorf. 2008. Rocking stability of masonry arches in seismic

regions. *Earthquake Spectra* 24 (4):847–65. doi:10.1193/1.2985763.

DeJong, M. J., and E. G. Dimitrakopoulos. 2014. Dynamically equivalent rocking structures. *Earthquake Engineering & Structural Dynamics* 43 (10):1543–63. doi:10.1002/eqe.2410.

DeJong, M. J., and J. A. Ochsendorf. 2006. Analysis of vaulted masonry structures subjected to horizontal ground motion. In *Proceedings, Fifth International Conference on the Structural Analysis of Historical Constructions*, ed. P. B. Lourenco, P. Roca, C. Modena, and S. Agrawal, 973–80. New Delhi.

De Lorenzis, L., M. J. DeJong, and J. A. Ochsendorf. 2007. Failure of masonry arches under impulse base motion. *Earthquake Engineering & Structural Dynamics* 36 (14):2119–36. doi:10.1002/eqe.

Dimitrakopoulos, E. G., and M. J. DeJong. 2012. Revisiting the rocking block: Closed-form solutions and similarity laws. *Proceedings of the Royal Society A: Mathematical, Physical and Engineering Sciences* 468 (2144):2294–318. doi:10.1098/rspa.2012.0026.

DMI. 2008. Decreto Del Ministro Delle Infrastrutture 14 Gennaio 2008. Approvazione Delle Nuove Norme Tecniche per Le Costruzioni. Gazzetta Ufficiale Della Repubblica Italiana n. 29, Supplemento Ordinario n. 30.

Doherty, K., M. C. Griffith, N. T. K. Lam, and J. L. Wilson. 2002. Displacement-based seismic analysis for out-of-plane bending of unreinforced masonry walls. *Earthquake Engineering & Structural Dynamics* 31 (4):833–50. doi:10.1002/eqe.126.

EN 1998-1. 2004. *Eurocode 8. Design of structures for Earthquake resistance—part 1: General rules, seismic actions and rules for buildings*. Brussels, Belgium: CEN.

Ferrante, A., F. Clementi, and G. Milani. 2020. Advanced numerical analyses by the non-smooth contact dynamics method of an ancient masonry bell tower. *Mathematical Methods in the Applied Sciences* 43 (13):7706–25. doi:10.1002/mma.6113.

Ferrante, A., D. Loverdos, F. Clementi, G. Milani, A. Formisano, S. Lenci, and V. Sarhosis. 2021. discontinuous approaches for nonlinear dynamic analyses of an ancient masonry tower. *Engineering Structures* 230:111626. doi:10.1016/j.engstruct.2020.111626.

Giresini, L., and M. Sassu. 2017. Horizontally restrained rocking blocks: evaluation of the role of boundary conditions with static and dynamic approaches. *Bulletin of Earthquake Engineering* 15 (1):385–410. doi:10.1007/s10518-016-9967-7.

Heyman, J. 1992. Leaning towers. *Meccanica* 27 (3):153–59. doi:10.1007/BF00430041.

Housner, G. W. 1963. The behavior of inverted pendulum structures during Earthquakes. *Bulletin of the Seismological Society of America* 53 (2):403–17. doi:10.1785/BSSA0530020403.

Iwan, W. D., and X. D. Chen. 1994. Important near-field ground motion data from the landers Earthquake. In *Proceedings, 10th European Conference on Earthquake Engineering*, ed. G. Duma. Rotterdam.

Klöckner, A. 2008. MeshPy. https://pypi.org/project/MeshPy/

Lachanas, C. G., and D. Vamvatsikos. 2022. Rocking incremental dynamic analysis. *Earthquake Engineering and Structural Dynamics* 51 (3):688–703. doi:10.1002/eqe.3586.

Lagomarsino, S. 2015. Seismic assessment of rocking masonry structures. *Bulletin of Earthquake Engineering* 13 (1):97–128. doi:10.1007/s10518-014-9609-x.

Liew, A., and T. Mendez Echenagucia. 2017. compas_fea: Finite element analysis package for the COMPAS framework. https://compas.dev/compas_fea/latest/

Makris, N., and Y. Roussos. 1998. Rocking response and overturning of equipment under horizontal pulse-type motions. Report No. PEER-98/05, Pacific Earthquake Engineering Center, University of California, Berkeley. Accessed August 11, 2022. https://apps.peer.berkeley.edu/publications/peer_reports/reports_1998/9805.pdf

Makris, N., and Y. Roussos. 2000. Rocking response of rigid blocks under near-source ground motions. *Geotechnique* 50 (3):243–62. doi:10.1680/geot.2000.50.3.243.

Makris, N., and M. F. Vassiliou. 2013. Planar rocking response and stability analysis of an array of free-standing columns capped with a freely supported rigid beam. *Earthquake Engineering & Structural Dynamics* 42 (3):431–49. doi:10.1002/eqe.2222.

Malomo, D., M. J. DeJong, and A. Penna. 2021. Influence of bond pattern on the in-plane behavior of URM piers. *International Journal of Architectural Heritage* 15 (10):1492–511. doi:10.1080/15583058.2019.1702738.

Mauro, A., G. de Felice, and M. J. DeJong. 2015. The relative dynamic resilience of masonry collapse mechanisms. *Engineering Structures* 85:182–94. doi:10.1016/j.engstruct.2014.11.021.

McKenna, F., G. L. Fenves, M. H. Scott, and B. Jeremic. 2000. Open system for Earthquake engineering simulation (OpenSees).

Mehrotra, A., and M. J. DeJong. 2017. The performance of slender monuments during the 2015 Gorkha, Nepal, Earthquake. *Earthquake Spectra* 33 (S1):321–43. doi:10.1193/120616EQS223M.

Mehrotra, A., and M. J. DeJong. 2018. A CAD-interfaced dynamics-based tool for analysis of masonry collapse mechanisms. *Engineering Structures* 172:833–49. doi:10.1016/j.engstruct.2018.06.053.

Milani, G., and F. Clementi. 2021. Advanced seismic assessment of four masonry bell towers in Italy after Operational Modal Analysis (OMA) Identification. *International Journal of Architectural Heritage* 15 (1):157–86. doi:10.1080/15583058.2019.1697768.

OPCM. 2006. Ordinanza Del Presidente Del Consiglio Dei Ministri 28 Aprile 2006. Criteri Generali per l'individuazione Delle Zone Sismiche e per La Formazione e l'aggiornamento Degli Elenchi Delle Medesime Zone. (Ordinanza n. 3519).

Oppenheim, I. J. 1992. The masonry arch as a four-link mechanism under base motion. *Earthquake Engineering & Structural Dynamics* 21 (11):1005–17. doi:10.1002/eqe.4290211105.

Pacific Earthquake Engineering Research Center (PEER). 2014. PEER ground motion database. https://ngawest2.berkeley.edu/site

PCM-DPC MiBAC. 2006. Model A-DC Scheda per Il Rilievo Del Danno Ai Beni Culturali - Chiese.

Peña, F., P. B. Lourenço, N. Mendes, and D. V. Oliveira. 2010. Numerical models for the seismic assessment of an old masonry tower. *Engineering Structures* 32 (5):1466–78. doi:10.1016/j.engstruct.2010.01.027.

Priestley, M. J. N. 1985. Seismic behaviour of unreinforced masonry walls. *Bulletin of the New Zealand Society for Earthquake Engineering* 18 (2):191–205. doi:10.5459/bnzsee.18.2.191-205.

Pulatsu, B., F. Gencer, and E. Erdogmus. 2020. Study of the effect of construction techniques on the seismic capacity of ancient dry-joint masonry towers through DEM. *European Journal of Environmental and Civil Engineering* 26 (9):3913–30. doi:10.1080/19648189.2020.1824823.

Robert McNeel & Associates. 2014. Rhinoceros 5.

Sarhosis, V., G. Milani, A. Formisano, and F. Fabbrocino. 2018. Evaluation of different approaches for the estimation of the seismic vulnerability of masonry towers. *Bulletin of Earthquake Engineering* 16 (3):1511–45. doi:10.1007/s10518-017-0258-8.

Shakya, M., H. Varum, R. Vicente, and A. Costa. 2018. Seismic vulnerability assessment methodology for slender masonry structures. *International Journal of Architectural Heritage* 12 (7–8):1297–326. doi:10.1080/15583058.2018.1503368.

Shehu, R. 2022. Preliminary assessment of the seismic vulnerability of three inclined bell-towers in Ferrara, Italy. *International Journal of Architectural Heritage* 16 (4):485–517. doi:10.1080/15583058.2020.1805045.

Si, H. 2015. TetGen, a Delaunay-based quality tetrahedral mesh generator. *ACM Transactions on Mathematical Software* 41 (2):Article 11. doi:10.1145/2629697.

Sorrentino, L., S. Kunnath, G. Monti, and G. Scalora. 2008. Seismically induced one-sided rocking response of unreinforced masonry facades. *Engineering Structures* 30 (8):2140–53. doi:10.1016/j.engstruct.2007.02.021.

Sorrentino, L., R. Masiani, and M. C. Griffith. 2008. The vertical spanning strip wall as a coupled rocking rigid body assembly. *Structural Engineering and Mechanics* 29 (4):433–53. doi:10.12989/sem.2008.29.4.433.

Torelli, G., D. D'Ayala, M. Betti, and G. Bartoli. 2020. Analytical and numerical seismic assessment of heritage masonry towers. *Bulletin of Earthquake Engineering* 18 (3):969–1008. doi:10.1007/s10518-019-00732-y.

Valente, M., and G. Milani. 2016a. Non-linear dynamic and static analyses on eight historical masonry towers in the North-East of Italy. *Engineering Structures* 114:241–70. doi:10.1016/j.engstruct.2016.02.004.

Valente, M., and G. Milani. 2016b. Seismic assessment of historical masonry towers by means of simplified approaches and standard FEM. *Construction and Building Materials* 108:74–104. doi:10.1016/j.conbuildmat.2016.01.025.

Van Mele, T., and Many Others. 20172021. COMPAS: A framework for computational research in architecture and structures. doi:10.5281/zenodo.2594510.